The central energy source of 70 μm-selected galaxies: starburst or AGN?

M. Symeonidis,[1]⋆ D. Rosario,[2] A. Georgakakis,[3] J. Harker,[2] E. S. Laird,[4] M. J. Page[1] and C. N. A. Willmer[5]

[1]*Mullard Space Science Laboratory, University College London, Holmbury St. Mary, Dorking, Surrey RH5 6NT*
[2]*Astronomy and Astrophysics, 201 Interdisciplinary Sciences Building, Santa Cruz, CA 95064, USA*
[3]*National Observatory of Athens, Institute of Astronomy, V. Paulou and I. Metaxa, Athens 15236, Greece*
[4]*Imperial College London, Blackett Laboratory, Prince Consort Road, London SW7 2AZ*
[5]*Steward Observatory, University of Arizona, 933 North Cherry Avenue, Tuscon, AZ 85721, USA*

ABSTRACT

We present the first active galactic nuclei (AGN) census in a sample of 61 galaxies selected at 70 μm, a wavelength which should strongly favour the detection of star-forming systems. For the purpose of this study, we take advantage of deep *Chandra* X-ray and *Spitzer* infrared (3.6–160 μm) data, as well as optical spectroscopy and photometry from the Deep Extragalactic Evolutionary Probe 2 (DEEP 2) survey for the Extended Groth Strip (EGS) field, as part of the All-Wavelength Extended Groth Strip International Survey. We investigate spectral line diagnostics ([O III]/Hβ and [Ne III]/ [O II] ratios, Hδ Balmer absorption line equivalent widths and the strength of the 4000 Å break), X-ray luminosities and spectral energy distributions (SEDs). We find that the 70-μm sources are undergoing starburst (SB) episodes and are therefore characterized by a predominance of young stars. In addition, 13 per cent of the sources show AGN signatures and hence potentially host an AGN. When the sample is split into SBs ($10^{10} < L_{IR} < 10^{11}$ L$_\odot$), luminous infrared Galaxies (LIRGs; $10^{11} < L_{IR} < 10^{12}$ L$_\odot$) and ultraluminous infrared Galaxies (ULIRGs; $10^{12} < L_{IR} < 10^{13}$ L$_\odot$), the AGN fraction becomes 0, 11 and 23 per cent, respectively, showing an increase with total infrared luminosity. However, by examining the sources' panchromatic SEDs, we conclude that although the AGN is energetically important in 1 out of 61 objects all 70-μm-selected galaxies are primarily powered by star formation. When compared to a sample of DEEP 2 galaxies in the same redshift range and with similar optical colours, we find that the 70-μm population is characterized by younger stellar ages and a higher AGN incidence, indicating that strongly star-forming populations might be a key in studying the relationship between black hole and stellar growth.

Key words: galaxies: active – galaxies: general – galaxies: high-redshift – galaxies: starburst – infrared: galaxies – X-rays: galaxies.

1 INTRODUCTION

Understanding the relationship and relative contribution of the fundamental energy sources in the Universe, active galactic nuclei (AGN) accretion and star formation, is far from trivial. Data from three generations of infrared (IR) observatories, *IRAS*, *Infrared Space Observatory* (*ISO*) and *Spitzer*, have revealed that the most powerful activity in the Universe is dust enshrouded. Obscured galaxies are responsible for roughly half the cosmic energy density originating from stars and AGN: the cosmic infrared background (CIRB). Observational and theoretical results have placed the history of star formation and black hole accretion in parallel evolutionary paths, linked to the close relationship between central black holes and galaxy properties (Magorrian et al. 1998), a key aspect of identifying the processes that drive galaxy evolution (e.g. Sanders et al. 1988; Norman & Scoville 1988; Rowan-Robinson & Crawford 1989; Rowan-Robinson 1995), with speculations of a complex two-way feedback method whereby AGN and starburst (SB) activity is inter-regulated (e.g. Umemura, Fukue & Mineshige 1997; Appleton et al. 2002; King 2005; Springel, Di Matteo & Hernquist 2005). Although disentangling the relative SB/AGN contributions to the IR energy budget is key for identifying the processes that drive galaxy evolution, such a task has proved extremely challenging and any substantial progress has been slowed by the difficulty of identifying obscured AGN at high redshift. The presence

⋆E-mail: msy@mssl.ucl.ac.uk

of dust in the host galaxy complicates matters further, as the relative contribution of stars and AGN to the bolometric luminosity becomes an elusive quantity.

The main contributors to the CIRB, luminous and ultraluminous infrared Galaxies (LIRGs and ULIRGs), are characterized by large amounts of dust, emission from which completely dominates their energetic output. As dust grain formation and destruction are a dynamical, stellar-related process with the lifetime of a typical grain of the order of a few hundred Myr (Draine 2003), the presence of large amounts of dust combined with a high-IR output implies rapid, ongoing star formation and/or intense SB episodes. With data from the Multiband Imaging Photometer for *Spitzer* (MIPS), the properties of these populations have been examined out to $z \sim 2$; however, it is only with the far-IR (70 and 160 µm) bands that greater relevance to star formation can be achieved, as they probe nearer the spectral energy distribution (SED) peak of a star-forming galaxy ($\sim$40–150 µm). Because of its higher sensitivity, the MIPS 70-µm band has been more widely exploited than the 160-µm band, with 70-µm populations found to predominantly consist of IR-luminous ($L_{IR} > 10^{10}$) and dust-rich objects, mainly in the $0.1 \lesssim z \lesssim 1.5$ redshift range (Symeonidis et al. 2008, 2009, hereafter S08, S09). As a result, setting the initial sample selection at 70 µm is ideal for studying the relationship (if any) between obscured star formation and supermassive black hole growth, as well as evaluating the degree of coeval activity between AGN and star formation during a galaxy's lifetime.

Numerous studies have revealed that a large part of the bolometric luminosity in IR-luminous sources could originate from AGN in some cases prevailing over the SB output (e.g. Gregorich et al. 1995; Genzel et al. 1998; Tacconi et al. 2002), with the AGN contribution seen to increase as a function of total IR luminosity (e.g. Lutz et al. 1998; Fadda et al. 2002; Brand et al. 2006). Identifying the presence of AGN in obscured galaxies requires the combination of various disgnostics such as mid-IR colours (e.g. Lacy et al. 2004; Stern et al. 2005; Barmby et al. 2006), SED shape (e.g. Alonso-Herrero et al. 2006), X-ray luminosity (e.g. Pompilio, La Franca & Matt 2000) and radio luminosity (e.g. Donley et al. 2005). Optical spectrosopy is also a powerful tool (e.g. Osterbrock 1989; Tresse et al. 1996; Takata et al. 2006), with recent evidence pointing towards evolutionary differences, rather than solely orientation effects (e.g. Antonucci 1993), being responsible for the variety of AGN spectroscopic signatures (e.g. Hasinger 2008), resulting in a mixture of both type I and II spectra. In addition to the traditional 'torus-obscured' AGN, studies have revealed the potential of 'host-obscured' AGN as a plausible scenario, where light from the nucleus is also obscured by the dusty star-forming host galaxy (e.g. Martínez-Sansigre et al. 2006). For such sources, optical spectroscopy is a powerful diagnostic with a plethora of emission lines both from the AGN and host, providing important clues on the environments in which they originate (e.g. Brand et al. 2007). 70-µm populations are at a considerable advantage for multiwavelength spectroscopic and photometric follow-up: the sensitivity of the MIPS 70-µm band is such that only the brightest sources are selected at each redshift and hence are very likely to have counterparts over a wide wavelength range. Moreover, the redshift distribution of 70-µm populations allows many key emission and absorption lines to be within a typical optical grating range.

Due to the effects of dust obscuration, AGN censuses in IR and sub-mm populations have mainly been approached through mid-IR and X-ray surveys (e.g. Vignati et al. 1999; Almaini, Lawrence & Boyle 1999; Fabian, Wilman & Crawford 2002; Alexander et al. 2005; Martínez-Sansigre et al. 2005; Matute et al. 2006). X-ray

surveys have resolved most of the 0.5–10 keV cosmic X-ray background (CXRB) and attributed it to emission from accreting supermassive black holes (e.g. Shanks et al. 1991); however, lack of sensitivity has not allowed the detection of the majority of extragalactic X-ray sources contributing at low ($<10^{-16}$ erg s^{-1} cm^{-2}) fluxes. These are most likely high-redshift, star-forming and SB galaxies, possibly containing low-luminosity or deeply obscured AGN (e.g. Ptak et al. 2003; Franceschini et al. 2003, hereafter F03; Bauer et al. 2004; Brandt & Hasinger 2005). A large obscured AGN population has long been predicted from both statistical analysis and number counts of AGN samples as well as from CXRB models (e.g. Comastri et al. 1995; Worsley et al. 2005), especially since the steep broad-line quasi-stellar object (QSO) spectrum cannot explain the intensity of the hard X-ray background (e.g. Fabian et al. 1998). This implies that most accretion-generated energy density in the Universe takes place in obscured objects, making obscured AGN the main candidates for the origin of the hard CXRB, which peaks at $\sim$30 keV and, as yet, has not been resolved (e.g. Setti & Woltjer 1989; Fabian & Iwasawa 1999).

The aim of this paper is to examine the AGN content of a sample of IR-luminous 70-µm-selected galaxies from the Extended Groth Strip (EGS) field. We combine *Chandra* X-ray data and optical spectroscopy in order to constrain the AGN fraction and identify the dominant process responsible for the sources' total energy budget. Section 2 introduces the sample and gives an analysis of IR/optical colours. In Section 3, we examine the sample's X-ray properties, whereas in Section 4 the analysis focuses on optical spectra and emission line ratios. The AGN contribution is discussed in Section 5 and our summary and conclusions are presented in Section 6. Throughout, we employ $H_0 = 70$ km s^{-1} Mpc^{-1}, $\Omega_M = 0.3$ and $\Omega_\Lambda = 0.7$ (Spergel et al. 2003).

2 THE SAMPLE

2.1 Initial selection and previous work on the 70 − µm sample

This work is based on Guaranteed Time Observations of the EGS field ($\sim$0.5 deg^2) (Davis et al. 2007) by *Spitzer's* (Werner et al. 2004) far-IR photometer MIPS (Rieke et al. 2004). The initial selection was made at 70 µm, where 178 sources were retrieved down to $\sim$4 mJy (5σ), with photometric completeness at $\sim$10 mJy. We focus on a subset of this population, the 114 sources in the overlap areas of the MIPS 24, 70, 160 µm and Infrared Array Camera (IRAC) 8-µm images and further narrow our working sample to 61 sources with optical photometry and spectroscopic redshifts from the Deep Extragalactic Evolutionary Probe 2 (DEEP 2) survey (Davis et al. 2003; see Section 2.2). The MIPS 70-µm catalogue was cross-correlated to the MIPS 24 µm and IRAC catalogues in two steps: first, using a $\sim$10-arcsec radius for the MIPS70/MIPS24 matching and subsequently using a $\sim$2.5 arcsec radius for the MIPS24/IRAC matching. For data reduction and source extraction, we refer the reader to Symeonidis et al. (2007, hereafter S07; S08; S09), where the IR properties of the 70-µm sample were also examined in detail. A succinct summary of our results from previous work follows.

In S08 and S09, we fitted the available IR photometry (8–160 µm) with the Siebenmorgen & Krügel (2007) templates and obtained estimates for the total IR luminosity (L_{IR}) in the 8–1000 µm range. We found characteristic luminosities of IR-luminous galaxies between 10^{10} and 10^{14} L$_\odot$, of which $\sim$11 per cent are SBs ($10^{10} < L_{IR} < 10^{11}$), $\sim$62 per cent are LIRGs ($10^{11} < L_{IR} < 10^{12}$) and $\sim$26 per cent are ULIRGS ($10^{12} < L_{IR} < 10^{13}$). We also identified one hyperluminous infrared Galaxy (HyLIRG; $L_{IR} > 10^{13}$) at

$z = 1.9$, which we remove from subsequent analysis as it is unique and will be treated separately in a later paper. The optical/IR SEDs for all, but one, objects are SB type, with a strong optical/near-IR stellar bump, an inflection in the near-IR and elevated flux in the IR. One object, identified with red near-IR colours in all IRAC colour bands, has an SED that shows an elevated near-IR power-law continuum instead of an inflection in that region (see Sections 5 and 5.1). Infrared and radio derived star formation rates (SFRs) were calculated in S07 and were found to be in the $\sim$5–1000 $M_\odot$ yr^{-1} range, with the majority of the objects having SFR > 50 $M_\odot$ yr^{-1}. SFRs calculated using optical emission lines not corrected for dust extinction, on average fell short by a factor of 50, implying that the optical part of the spectrum is not an accurate tracer of star formation in these systems, especially since in addition to high extinction IR-luminous sources will likely host deeply embedded star-forming regions that do not contribute at all to the optical energy budget.

2.2 Optical selection

The EGS benefits from extensive observational coverage via the All-Wavelength Extended Groth Strip International Survey (AEGIS), which provides optical spectroscopy and multiwavelength photometry over an area of $\sim$1 deg^2 (see Davis et al. 2007 for a summary of the AEGIS photometric data sets). From the 114 objects with IR photometry, we select 109 with area coverage in the *B*, *R*, *I* bands, from the DEEP 2 Survey (Coil et al. 2004; Faber et al., in preparation). Taking advantage of IRAC's high positional accuracy ($\sim$0.1 arcsec), we cross-correlate the 70-μm sample with DEEP 2 using the IRAC coordinates for our sources and an appropriate matching radius of $\lesssim$1.5 arcsec corresponding to IRAC's pixel size. Currently, $\sim$75 per cent of the MIPS 70-μm strip is covered by DEEP 2 and this will increase to 100 per cent with the DEEP 3 cycle of observations. Where possible, we also supplement our data set with photometry from the Galaxy Evolution Explorer (GALEX), the Palomar wide-field infrared camera and the Canada–France–Hawaii Telescope Legacy Survey in the far-UV, near-UV, *g, r, i, z, J* and *K* bands and *Spitzer's* IRAC in the 3.6-, 4.5- and 5.8-μm bands.

Apart from the exclusion of stars, the photometric part of DEEP 2 did not pose any constraints on the EGS. On the other hand, the spectroscopic part of DEEP 2 targeted sources only within the $18.5 < R < 24.1$ (AB) magnitude range. Although the retrieval of redshifts was random at $\sim$60 per cent sampling, a weighting scheme was applied, giving lower weights to $z < 0.75$ objects in order to sample a wide range of luminosities and roughly equal numbers of galaxies below and above $z = 0.75$; see Faber et al. (2007), Davis et al. (2007). For a reliable redshift, two significant features, such as the [O II] doublet, were required in order to provide a match and hence most redshift failures were from high-redshift objects ($z > 1.4$) which did not have strong features in the DEEP 2 spectral range. At the time of writing there are 62 good-quality redshifts and spectra available for the 70-μm EGS population, in the $0.17 < z < 1.9$ range, with a mean of 0.57 and a median of 0.48. Note that we remove the HyLIRG from the redshift sample (see Section 2.1) with the final number of sources being 61. Hereafter, the term '70-μm sample' refers only to the sources with redshifts.

In Fig. 1, we compare the *R*-band magnitude distribution of the redshift sample to the sources with no redshifts. Although there is high overall consistency, a few differences are evident originating from the spectroscopic selection criteria outlined earlier. First, there is an under-representation of bright sources: there are 10 $R < 18.5$ sources in total and, at 60 per cent redshift sampling, $\sim$6 of those should have made it in the redshift sample. The *R*-band – redshift
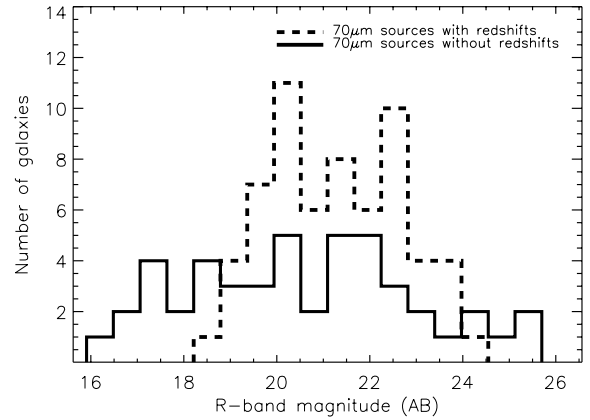

Figure 1. The *R*-band magnitude distribution for the 109 70-μm sources – solid line: the 47 sources without redshifts; dashed line: the 61 objects with DEEP 2 redshifts. The exclusion of the brightest sources and spectroscopic weighting scheme, cause discrepancies in the two distributions at the faint and bright ends.
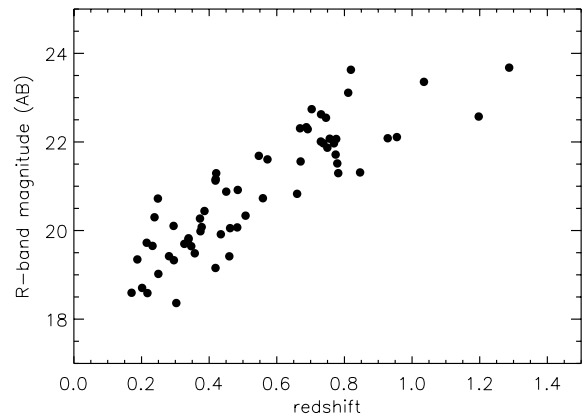
Figure 2. *R*-band magnitude versus redshift.
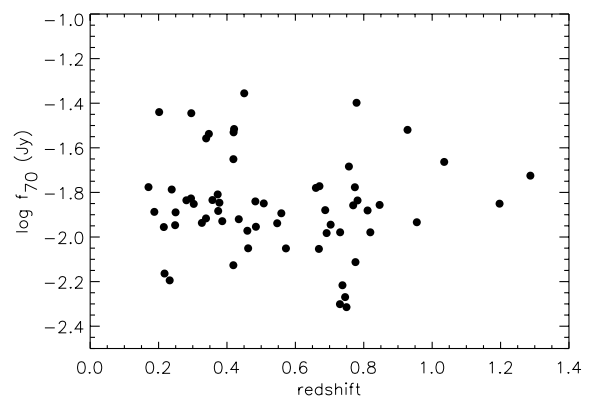
Figure 3. 70-μm flux density versus redshift.

relation (Fig. 2) shows that these are at low redshift. Secondly, on the faint end, there are four objects fainter than $R = 24.1$ in the full sample, i.e. two to three should have also appeared in the redshift sample. The effects of the spectroscopic selection are further examined in Fig. 3, where the 70-μm flux density (f_{70}) is plotted as a function of redshift. In contrast to the clear $R - z$ relation (Fig. 2), f_{70} does not show signs of a trend with redshift, implying
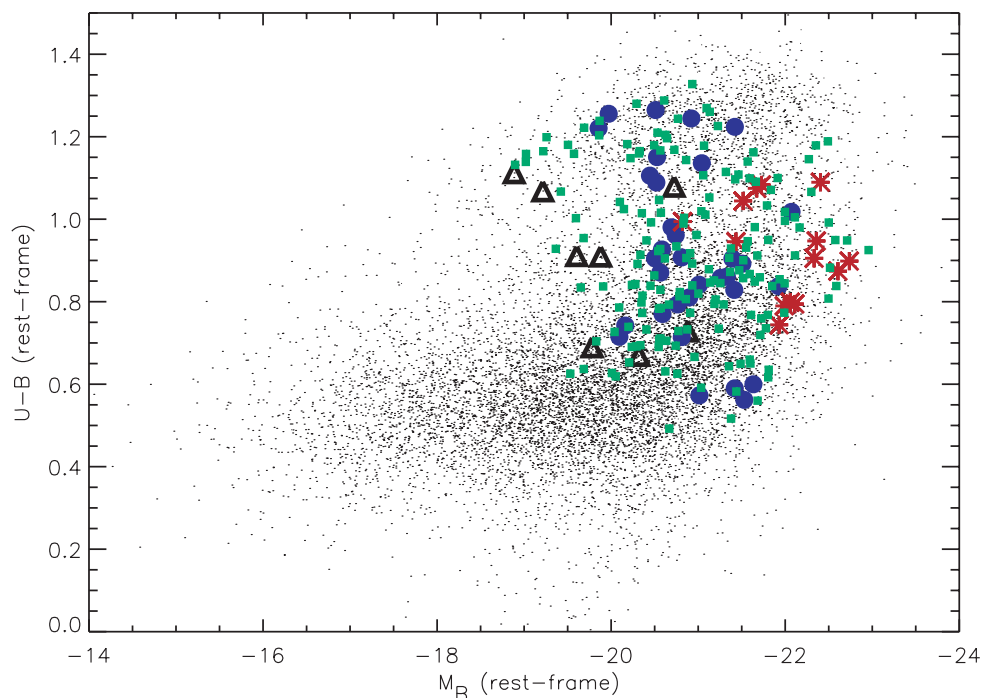
Figure 4. $U - B$ colours versus absolute B magnitude, M_B (AB), with the 70-µm sample in black open triangles, blue filled circles and red asterisks (SBs, LIRGs and ULIRGs, respectively) and the control sample as green filled squares. All ~11 000 EGS sources from the DEEP 2 spectroscopic survey are shown in the background as black points.

Figure 5. The redshift distribution of the 70-µm sample (red solid line) and the control sample (black dashed line).

that the DEEP 2 spectroscopic criteria do not have any affect on the IR properties of the 70-µm sample.

2.3 The control sample

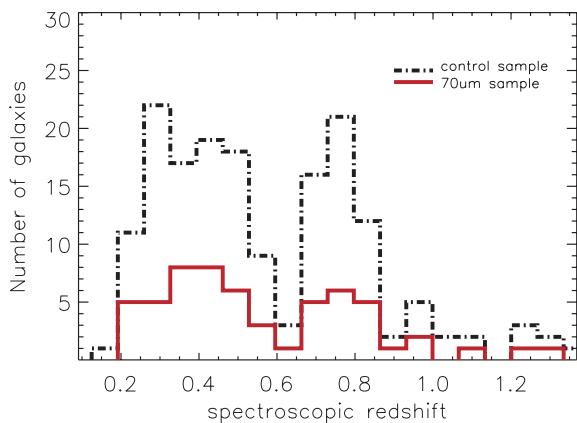Due to the unique nature of the 70-µm population (see Section 2.1) and as this work focuses on determining the AGN fraction, it is more insightful to do so in relation to galaxies of comparable properties in a similar redshift range. With that in mind, we assemble a control sample of DEEP 2 EGS sources: for each 70-µm galaxy with a DEEP 2 redshift, we find up to three others with comparable redshifts, rest-frame B-band luminosities and $U - B$ colours (see Willmer et al. 2006 for a discussion of K-corrections) – 'comparable' is quantified as $\Delta z \leq 0.03$, $\Delta M_B \leq 0.4$ and $\Delta(U - B) \leq 0.1$ (see Figs 4 and 5).

Fig. 4 shows the variation of $U - B$ colour versus M_B (AB) – the colour–magnitude diagram (CMD) – for the control and 70-µm sample; the colour distribution for all EGS sources in the DEEP 2 spectroscopic survey is also shown in the background. The CMD represents galaxy evolution from the blue cloud – young stellar content – to the red sequence – evolved stellar populations – associated with morphological changes from spirals to ellipticals and mediated by a transitional green valley stage (e.g. Bell et al. 2004). The 70-µm sample is bright in the optical but has red $U - B$ colours; there is substantial contribution to the red sequence, but more sources seem to be in the upper blue cloud/green valley region.

An alternative way to select the control sample could be by stellar mass. However, due to lack of complete optical/near-IR data sets for the EGS, mass information for the DEEP 2 galaxies (see Conselice et al. 2007) is only available for about 64 per cent of the 70-µm population. The subset of 70-µm objects with available stellar masses is characterized by a narrower distribution of higher average mass ($\langle \log M \rangle = 10.87$), compared to the control galaxies ($\langle \log M \rangle = 10.23$) (C. Conselice, private communication). The stellar mass distribution of the 70-µm galaxies is consistent with previous studies of IR galaxies (e.g. Caputi et al. 2006a,b) and comparable to those of early-types in the $z < 1$ redshift range (e.g. Ferreras et al. 2009). For our purpose, colour/magnitude selection of the control sample is more appropriate than stellar mass, because (i) stellar masses are not available for the whole 70-µm sample and (ii) colour/magnitude selection avoids a control sample dominated by high-mass evolved galaxies with little or no star formation.

Note that the optical luminosities and colours are not extinction corrected, which might imply that the intrinsic properties of the 70-µm sample could be better matched to objects in the more optically luminous part of the CMD or those whose red colours are principally a consequence of dust reddening rather than stellar age.

Table 1. Table of stacked fluxes (erg s^{-1} cm^{-2}) and hardness ratios for the 70-μm sample split into 3 luminosity classes (SBs, LIRGs and ULIRGs; see Section 2.1 for details on the sources' IR properties). The second column indicates how many objects were used in the stacking – some were removed either because they were too close to a source which could have contaminated the signal or they were associated with an X-ray source. The SB group does not have a formal detection in the hard band, so we quote the 3σ upper limit. The hardness ratio is derived using the counts in the soft band and 3σ upper limit counts in the hard band.

Class	Objects used	$f_{0.5-2}$	f_{2-10}	HR
SBs	eight out of 9	8.67E-17 (8σ)	2.51E-16 (3σ upper limit)	-0.3 (upper limit)
LIRGs	29 out of 35	5.04E-17 (9σ)	1.6E-16 (4σ)	-0.2
ULIRGs	9 out of 17	1.11E-16 (12σ)	1.84E-16 (3σ)	-0.5

Notwithstanding, the lack of correlation in Fig. 4 between $U - B$ colour and IR luminosity for the 70-μm sample implies that subsequent comparisons of each IR luminosity class with the respective control galaxies will be fair, since the latter span a large part of the CMD and hence a large range in properties.

2.4 X-ray data

The EGS was surveyed with the *Chandra* Advanced CCD Imaging Spectrometer to a depth of 200 ks, over an area of 0.67 deg^2 (Georgakakis et al. 2006; Davis et al. 2007; Laird et al. 2009, hereafter L09). The AEGIS X-ray survey and final data products are made available in L09. L09 describes the cross-matching between the DEEP 2 and X-ray AEGIS catalogues; we identify the X-ray counterparts of our 70-μm sample using DEEP 2 coordinates which were in turn matched to the IRAC coordinates of our sources (see Section 2.2). We use X-ray data in the soft (0.5–2 keV) and hard (2-10 keV) bands (flux limit of 1.1×10^{-16} and 8.2×10^{-16} erg s^{-1} cm^{-2}, respectively), choosing fluxes calculated using a Bayesian method, more reliable for faint sources as it corrects for the Eddington bias – for details on source extraction and flux estimation see L09.

Although the *Chandra* map covers the whole of the MIPS 70-μm strip, only about 16 per cent of the sources have individual X-ray detections (see Table 4). Estimates for the hardness ratio, calculated as $HR = \frac{H-S}{H+S}$, where H and S refer to the hard (2–7 keV) and soft (0.5–2 keV) count rates (counts s^{-1} cm^{-2}), are also shown. If there is only a detection in one band, HR is calculated using the 3σ upper limits. From the 61 sources in the sample, only 10 have a confirmed detection in the full band (0.5–8 keV), two of which are not detected in any further bands, four have detections only in the soft band, three in both the soft and hard bands and one in only the hard band. For the remaining objects, we performed stacking (see Table 1), after splitting the sample into three groups according to the total IR luminosity measurements. The *K*-corrected X-ray luminosities are calculated by assuming a photon index of $\Gamma = 1.9$ and the stacked fluxes are converted to luminosity using the mean redshift of the group, 0.22 for SBs, 0.5 for LIRGs and 0.87 for ULIRGs.

3 THE X-RAY/IR RELATION

Fig. 6 compares X-ray and IR luminosities for the 70-μm sample. Given that there are several sources of X-ray luminosity associated with stellar-related processes (e.g. X-ray binaries, supernova remnants, hot gas, SB-driven outflows), X-ray and IR emission are expected to be strongly correlated in star-forming galaxies (e.g. Fabbiano 1989; Griffiths & Padovani 1990; F03; Ranalli, Comastri & Setti 2003, hereafter RCS03), for which $L_{0.5-10\,\mathrm{keV}}$

ranges between 10^{40} and 10^{42} erg s^{-1} (Kim, Fabbiano & Trinchieri 1992a,b; Nandra et al. 2002; Laird et al. 2005). The boundaries between star formation and accretion typically extend over a couple of orders of magnitude, nonetheless a hard X-ray luminosity of $L_{2-10\,\mathrm{keV}} > 10^{42}$ erg s^{-1} is thought to be an indication that an AGN is the dominant emitter of X-rays (e.g. Georgakakis et al. 2007).

We evaluate the properties of our sources against the empirical soft and hard X-ray/IR relations derived for *IRAS* galaxies in the $9 < \log L_{60} < 11.5$ range from Griffiths & Padovani (1990) and for local star-forming SBs and LIRGs from RCS03, as well as the hard X-ray/IR relation derived for a sample of local ULIRGs from Franceschini et al. (2003, hereafter F03). From Fig. 6, it is clear that the survey limits are displaced from the star-forming relations by up to two orders of magnitude, suggesting that a 200 ks X-ray survey is not on average sensitive to distant star-forming galaxies and hence more likely to detect objects with a strong AGN contribution to their X-ray luminosity.

In the soft X-rays (Fig. 6, top panel), the AGN/ star formation separation is not clear: there is large scatter in $L_{0.5-2\,\mathrm{keV}}$, partly due to the fact that soft X-rays are subject to stronger attenuation by gas and dust, the degree of which is likely to vary from one system to another and as a result the contribution of the AGN to the soft X-rays may not be evident. In fact, even some of the ULIRGs in the F03 sample whose X-ray emission is classified as AGN dominated by F03 seem consistent with the star formation relations. On the other hand, the four sources detected in the hard X-rays (objects 59, 67, 83 and 122; Fig. 6, lower panel) have luminosities of $L_{2-10\,\mathrm{keV}} > 10^{42}$ erg s^{-1}, two to three orders of magnitude higher than expected from the IR–X-ray relation for star-forming systems, placing them into the AGN regime. Their luminosities lie between the hybrid/AGN F03 ULIRG sample and NGC 6240 (Vignati et al. 1999), in which the X-ray emission is associated with a binary AGN system. The hard X-ray luminosities of the remaining sources are consistent with both the RCS03 and F03 SB galaxies, as well as with the SB-dominated local ULIRG Arp220 (Iwasawa et al. 2001).

4 OPTICAL SPECTRA

Fig. 7 shows characteristic spectra for objects in the SB, LIRG and ULIRG luminosity classes ($< z > \sim$0.2, 0.5 and 0.8, respectively). The DEEP 2 spectral range, $\sim$6500–9000 Å, permits the following principal lines to be visible: [Ne III](λ3869), [O II] (λ3727) and Hδ(λ4102) at $0.6 \lesssim z \lesssim 1.8$, H$\alpha$ (λ6563) and [N II] (λ6584) at $z \lesssim 0.3$, Hβ(λ4861) and the [O III] doublet($\lambda\lambda$ 4959, 5007) at $0.3 \lesssim z \lesssim 0.8$. Emission line measurements (Table 4) were made by using single-Gaussian fits, after fitting the local stellar continuum with a linear combination of early-type and A-star spectral templates,
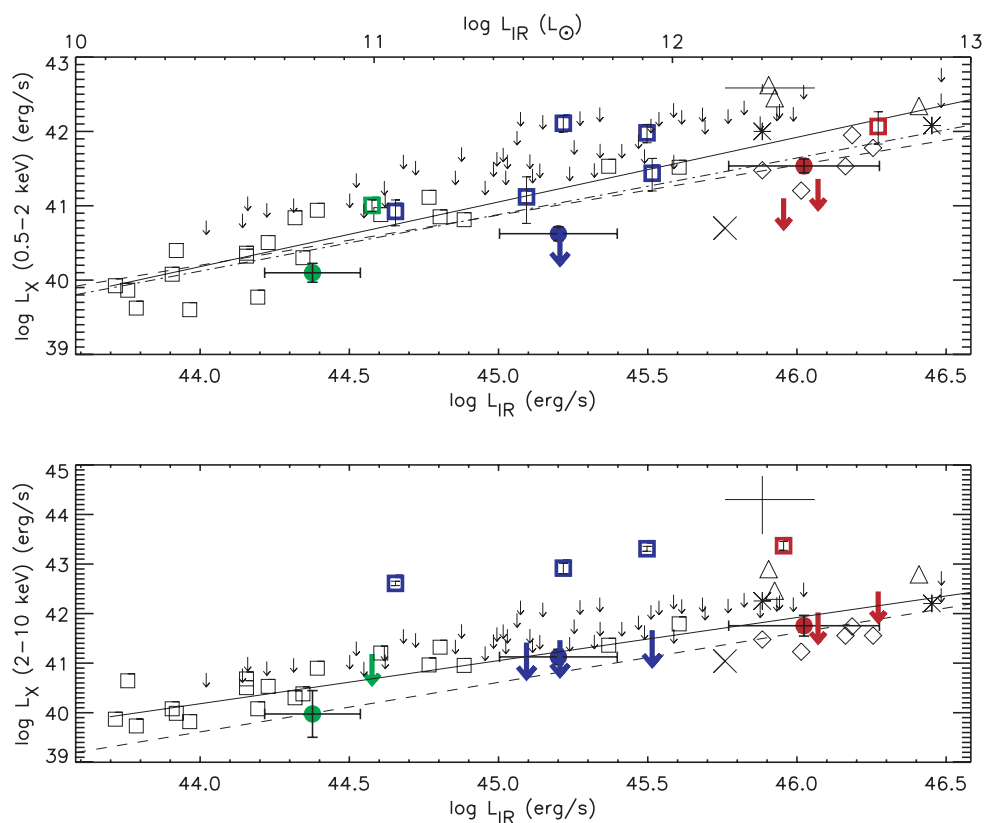
Figure 6. Soft (top panel) and hard (lower panel) X-ray luminosity (erg s^{-1}) versus L_{IR} (erg s^{-1} lower x-axis and L$_\odot$ upper x-axis) for the 70-μm sample. The colour scheme is green for SBs, blue for LIRGs and red for ULIRGs. Objects with a detection in at least one band have more reliable 3σ upper limits in other bands (large coloured symbols), whereas for the remaining sources the upper limits are calculated from the survey flux limits (see Section 2.4, black symbols). Filled circles correspond to luminosities calculated using the stacked 0.5–2 keV and 2–10 keV band flux and open squares are objects with X-ray detections. In the top panel, the lines are the star-forming relations from Griffiths & Padovani (1990) for SB /interacting galaxies (dashed line) and IRAS galaxies (dot-dashed line) and from Ranalli et al. (2003) for H ɪɪ galaxies (solid line). In the lower panel the lines indicate the star-forming relations from F03 (dashed line) for a sample of ULIRGs and Ranalli et al. (2003) for H ɪɪ galaxies (solid line). Overplotted is the ULIRG sample from F03; ULIRGs which are SB-dominated in the X-rays (diamonds), ULIRGs which are AGN dominated in the X-rays (triangles) and ULIRGs which are SB/AGN hybrids in the X-rays (asterisks). The open squares are the H ɪɪ galaxies from Ranalli et al. (2003). The small cross is Arp220 and the large vertical cross is NGC 6240, where the extent of the cross represents uncertainties in the luminosity.

to approximate the effects of absorption and continuum shape on the line strengths. This is particularly important for faint lines, such as [Ne ɪɪɪ], which lie in spectral regions with strong continuum substructure. Hδ equivalent widths (EWs) were derived using the model-fitting method of Harker et al. (in preparation): for the Balmer lines, the emission component, which comes from H ɪɪ regions, follows a well-defined decrement dependent only on the extinction in the ionized gas. The EWs of the absorption line component, determined by the mean stellar populations, are also well behaved across a range of star formation histories. By simultaneously measuring Hβ and Hδ in a spectrum, we are able to self-consistently estimate both emission and absorption line EWs for the $z \sim 0.6$–0.8 subset of 70-μm and control galaxies. In a similar way, Hβ emission lines were corrected for the underlying Hβ absorption component.

The diagnostic properties of emission lines, particularly useful when expressed in terms of line ratios, have found extensive use in determining conditions in the ISM, stellar ages, metallicity and the strength of the ionization field. As means of separating nuclear and stellar excitation processes, one of the most widely-used techniques, proposed by Baldwin, Phillips & Terlevich (1981, hereafter BPT), relies on identifying sources with respect to their [O ɪɪɪ]/Hβ and [N ɪɪ]/Hα ratios. As our sample spans a large redshift range, no

emission lines are common to the entire sample and as a result we cannot take advantage of such a diagnostic; there are no spectra with all four lines simultaneously visible. Hα is prominent in the $\langle z \rangle \sim 0.2$ SB population, also seen in the low-redshift LIRGs, but redshifted out of the spectral range at $z > 0.35$, where it gets replaced by emission from Hβ. The strong Hα and Hβ signatures in the galaxies' spectra are indicative of rapid ongoing star formation as they are directly related to the flux of massive stars ionizing the ISM (e.g. Kewley, Geller & Jansen 2004). We find no indication of Doppler-broadened (1000 $\lesssim$ FWHM $\lesssim$ 10 000 km s^{-1}) hydrogen lines suggestive of the presence of the broad-line region around an active nucleus. All sources with Hα in the spectral range also show the [N ɪɪ] feature; however, the latter is significantly weaker (e.g. see Fig. 7). We also identify the 4000 Å spectral break (D4000) and the higher order Balmer absorption line Hδ, associated with the age of stellar populations, in particular the presence of BAF class stars. D4000 was defined by Bruzual (1983) as the ratio of the average flux density in the 4050–4250 and 3750–3950 Å band, with the narrower equivalent (D_n4000: 4000–4100 to 3850–3950 Å) defined by Balogh et al. (1999). The existence of a break manifests a change in stellar opacity due to the accumulation of a large number of absorption lines from multiply ionized metals in the atmospheres
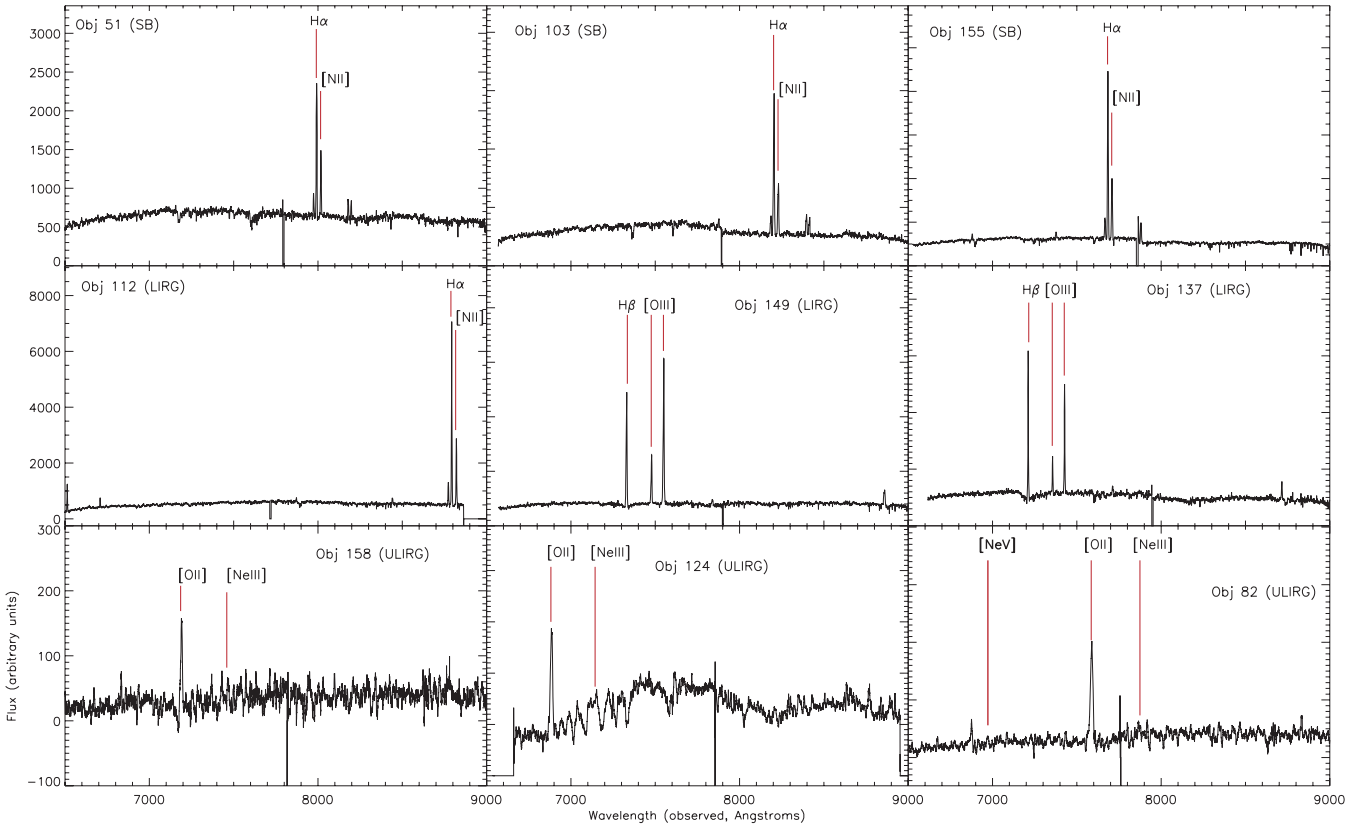
Figure 7. Characteristic spectra for the 70-μm sample, 3 SBs, 3 LIRGs and 3 ULIRGs.

of hot, metal-rich stars. Here, we calculate $D_n 4000$ as it is less sensitive to extinction, hence more appropriate for our sample, and investigate its strength in relation to the Balmer absorption line Hδ, both visible in the ~0.7–1.2 redshift range. However, as calculating Hδ EWs requires reliable Hβ measurements, we only have Hδ absorption line information for the eight objects in the sample for which both lines are in the accessible range (six LIRGs and two ULIRGs). Moreover, we are able to determine $D_n 4000$ for only seven out of 22 sources. For the remaining objects, we were not able to retrieve $D_n 4000$ measurements due to one or a combination of the following: one of the $D_n 4000$ bands being partially blanked by bad pixels, emission line contamination from [Ne III], there being no evidence of a break or lack of the reliable spectrograph throughput corrections.

Various common forbidden lines can also be seen in the spectra of the 70-μm sample, originating either in interstellar low-density PhotoDissociation Regions or the narrow-line region (NLR) in the vicinity of an AGN. The luminosity and ionization state of these lines is related to the strength of ionizing UV flux. More specifically, high-ionization states such as [NeV], which we detect in one object, are a consequence of a hard radiation field and hence unambiguous indicators of the presence of an AGN. The strong [O III] doublet appears in the $0.3 \lesssim z \lesssim 0.8$ spectral range. The 70-μm sources display various strengths of the [O III], [O II], [Ne III] and Hβ features and for the purpose of our study we are able to examine the [O III]/Hβ and [Ne III]/[O II] ratios for 33 70-μm sources in total.

In Sections 4.1–4.3, we examine the [O III]/Hβ and [Ne III]/[O II] ratios, as well as the behaviour of the Hδ absorption line and its relation to the 4000Å break and compare with equivalent measurements for the control galaxies matched to each 70-μm source. Note that

for all calculations we rely on flux ratios between features at similar wavelength, so the need for extinction correction is eliminated.

4.1 The [O III]/Hβ ratio

In traditional classification schemes (e.g. Ho, Filippenko & Sargent 1997), the [O III]/Hβ ratio has been used to distinguish SBs and Seyferts (e.g. Baldwin, Wampler & Burbridge 1981; Veilleux & Osterbrock 1987), with higher ratios found in hybrid AGN/SB galaxies (e.g. Caputi et al. 2008) and a typical [O III]/H$\beta > 3$ seen in Seyfert galaxies. Here, we are able to measure [O III]/Hβ for 20 LIRGs and eight ULIRGs from the 70-μm sample and associated control sources (Fig. 8). For the remaining sources one or both of these lines are out of range.

The LIRGs appear to have approximately the same log [O III]/Hβ mean value as the control galaxies (Fig. 8, top panel), roughly at -0.25, consistent with the line emission being linked to stellar processes, apart from two objects with [O III]/H$\beta > 5$. Five LIRGs have the Hβ emission line out of range, but the [O III] marginally in range; however, the latter is weak and not measurable in all but one object. In terms of the control sample, a tail-off to high [O III]/Hβ ([O III]/H$\beta > 3$) is evident, possibly due to Seyfert-types which are likely a few per cent of all galaxies at these redshifts. With respect to the ULIRGs (Fig. 8, lower panel), there is more spread in the two distributions, but with the 70-μm sample having higher mean [O III]/Hβ. Half the ULIRGs have [O III]/H$\beta < 3$, below the rough dividing line between AGN and star-forming galaxies and half have $3 < $ [O III]/H$\beta < 10$ typically seen in AGN. The five LIRGs and ULIRGs with [O III]/H$\beta > 3$ ratios are considered in subsequent work on the AGN fraction (Section 5).

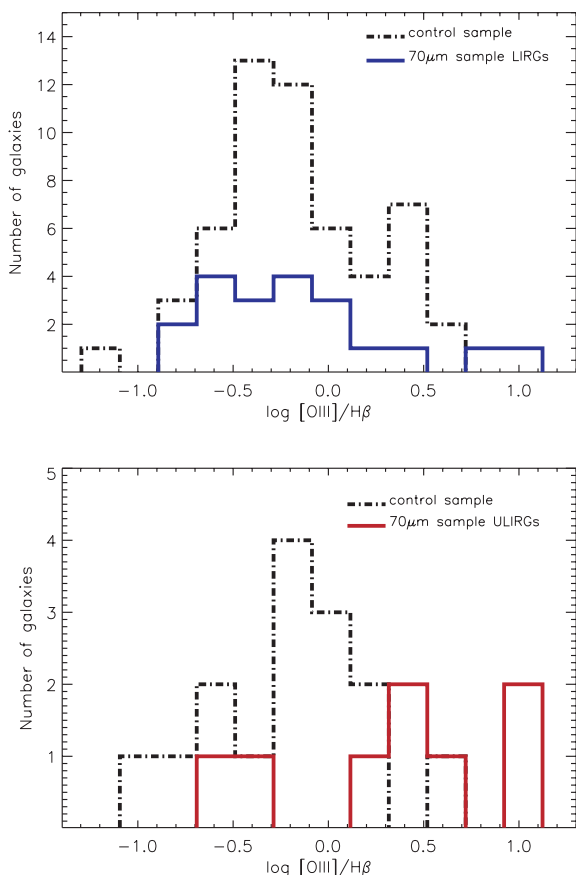**Figure 8.** Distribution of the [O III]/Hβ ratio for objects in the 70-μm sample (solid lines) – top panel for the LIRGs and lower panel for the ULIRGs – and their corresponding control galaxies (black dot-dashed lines).

Figure 9. Distribution of the [Ne III]/[O II] ratio for objects in the 70-μm sample (red solid line) and their respective control galaxies (black dot-dashed line).
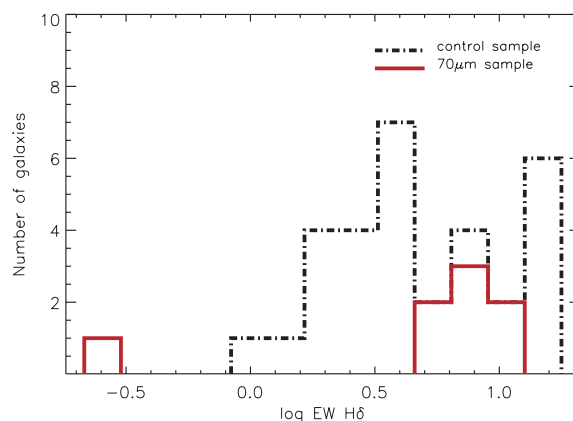
Figure 10. The distribution in Hδ absorption line EW. Red solid lines: the 7 sources from the 70μm sample which are in the right redshift range for reliable measurements (see Section 4). Black dot-dashed lines: their corresponding control galaxies.

4.2 The [Ne III]/[O II] ratio

The [Ne III]/[O II] ratio is a metallicity indicator, where the negative correlation with metallicity arises due to the atmospheres of more metal-rich stars absorbing a greater fraction of ionizing photons, softening the radiation field and decreasing the abundance of the higher ionization states (e.g. Nagao, Maiolino & Marconi 2006). [Ne III]/[O II] is also an ionization discriminator with AGN showing higher ratios on average, typically ∼0.4 for type 2 and >1 for type 1 (e.g. Nagao et al. 2002).

The [Ne III]/[O II] ratio for our sample can only be examined for the $z > 0.7$ sources, so all, apart from two, of the 10 sources with reliable measurements are ULIRGs (Table 4 and Fig. 9). The majority of the control galaxies are assembled between $-1.5 < \log [\text{Ne III}]/[\text{O II}] < -0.4$, which is the range one would expect for distant star-forming galaxies (e.g. Pérez-Montero et al. 2009), with two galaxies at $\log [\text{Ne III}]/[\text{O II}] > -0.5$, which are possibly Seyferts or metal poor. The 70-μm sources have $-1 < \log [\text{Ne III}]/[\text{O II}] < -0.2$ in two groups which peak at ∼-0.7 and ∼-0.3. The first group of five sources is in agreement with the average [Ne III]/[O II] ratio of the control sample. On the other hand, the peak at $\log [\text{Ne III}]/[\text{O II}] > -0.4$, occupied by the remaining five 70-μm sources, is degenerate as it is consistent with both a type 2 AGN regime (e.g. Nagao et al. 2002) and a low-metallicity regime (e.g. Pérez-Montero et al. 2007).

4.3 The Hδ absorption line and 4000 Å break

Fig. 10 compares the H δ absorption line for the seven sources from the 70-μm sample which are in the right redshift range to have good line measurements, to their respective control galaxies. The presence of higher order Balmer absorption lines is indicative of recent star-forming activity (e.g. Dressler & Gunn 1983), with the peak in Hδ absorption occuring at about ∼0.5 Gyr, followed by a decrease during the subsequent 1–10 Gyr epoch. The sources in our sample have higher Hδ EWs than the bulk of the control sample, implying a younger mean stellar population. Nevertheless, Hδ EWs in the 5–10 range are age degenerate, corresponding to systems that are either very young (∼10 Myr) or ∼1 Gyr old (e.g. Kauffmann et al. 2003, hereafter K03). To settle this degeneracy, we measure the narrow 4000 Å ($D_n 4000$) break and examine its strength against the Hδ absorption EW in Fig. 11. The 4000 Å break is a monotonic function of age, small for young stellar populations and large for old, metal-rich galaxies. We find that both the control and 70-μm sample lie where expected for star-forming galaxies with EW(Hδ) > 1 and $D_n 4000 > 1$; however, their spread over the $D_n 4000$-Hδ plane is substantially different: the control sample spans a large part of the plane, whereas the 70-μm sources have low $D_n 4000$ (<1.3) and most have high EW (Hδ) (>5) indicative of young stellar populations
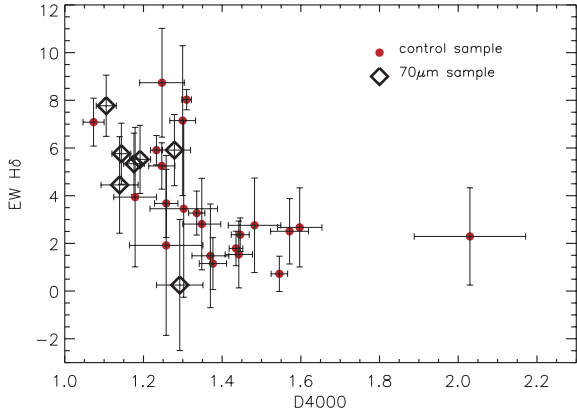
Figure 11. Plot of Hδ EW versus D_n4000. Red filled circles: the control sample, black diamonds: the 70-µm sample.

and consistent with an SB mode of star formation (e.g. K03). Similar values of D_n4000 and Hδ are also reported by Marcillac et al. (2006) and Caputi et al. (2008) who examine distant IR-selected galaxies. Caputi et al. (2008) find them to have the smallest D_n4000 values amongst a large sample of sources from the COSMOlogical evolution Survey, on par with the 70-µm sample occupying the lower end of the D_n4000 distribution of DEEP 2 control galaxies.

5 THE AGN CONTENT OF THE 70-µm POPULATION

5.1 The AGN fraction

In order to calculate the AGN fraction, we use four diagnostics – hard X-ray emission, high (>3) [O III]/Hβ ratio, the presence of [Ne v] lines and a power-law near/mid-IR continuum – with the requirement that at least one is satisfied for an object to be classed as an AGN candidate; see Table 2 and Figs 12 and 13.

The X-ray fraction in the 70-µm sample amounts to 16 (±6) per cent: two objects are detected in the full X-ray band only (objects 40 and 84), whereas eight have detections in at least one other band (objects 43, 56, 59, 67, 83, 93, 122 and 147). However, as star formation can also be a source of X-ray emission (see Section 3) we only consider sources with hard X-ray detections to be AGN candidates – objects 59, 67, 83 and 122 – especially since for the remaining sources X-ray emission is consistent with the star-forming relations in Fig. 6. These four sources also have $\log L_{2-10\,keV} > 42$,

which, as previously mentioned, usually indicates that hard X-ray emission is AGN dominated.

A power-law-type near/mid-IR ($3 \lesssim \lambda \lesssim 20\,\mu m$) continuum and hence red colours in that part of the SED are a consequence of emission from dust heated to near sublimation temperatures. As the strength of the stellar radiation field is not sufficient to cause this, the only stellar-related mechanism that could be responsible for a near/mid-IR excess is dust stochastically heated by shocks from outflows and supernovae (e.g. Ho et al. 1989; Davies, Burston & Ward 2002). However, studies have shown that the dust grains responsible are of very small size and hence lifetimes of the order of only a few kyr (Dwek 1986), making this an unlikely explanation for a near-IR excess in a broad-band SED. A more likely scenario is that of AGN dust heating and hence direct emission from the torus (Neugebauer et al. 1979; Elvis et al. 1994; Lutz et al. 1998; Sturm et al. 2000; Klaas et al. 2001; Alonso-Herrero et al. 2006). There is one object in the 70-µm sample with a power-law near/mid-IR continuum and red colours in all IRAC bands (3.6–8 µm) – object 165 (see SED in Fig. 13). It also has a high (>3) [O III]/Hβ ratio; see Table 2. The remaining AGN candidate sources have SB - type SEDs, although this does not exclude an AGN contribution to the near/mid-IR. In terms of AGN spectroscopic signatures, object 67 has an evident [Ne v] line and objects 84, 114, 141, 122, 165 have high [O III]/Hβ ratios (objects 67 and 122 are also hard X-ray emitters). Object 83, one of the hard X-ray emitters, has a spectrum that is almost devoid of emission lines, which implies complete obscuration or absence of the NLR and could be an example of a host-obscured source (e.g. Martínez-Sansigre et al. 2006), or a source with near 4π torus covering factor (Imanishi et al. 2007).

In total, eight out of 61 sources in the 70-µm sample show evidence for an active nucleus by satisfying at least one diagnostic, making the AGN fraction 13 per cent, or 11 and 23 per cent when the LIRGs and ULIRGs are considered seperately. Note that this is the fraction of sources which host an AGN, not the fraction of sources powered by AGN, and it is likely a lower limit, as it is possible that a number of AGN without spectroscopic or photometric signatures could be missed – see Section 5.3 for a discussion.

5.2 The AGN contribution to the energy budget

For the eight sources which are found to host an active nucleus, we investigate the AGN contribution to the total energy budget with the aid of SED templates; Fig. 13 shows the sources' panchromatic SEDs with X-ray fluxes in the hard and soft bands,

Table 2. The eight objects identified to host AGN. Columns 1–6: object ID, IR luminosity class, SED type, hard X-ray luminosity, the [O III]/Hβ ratio, a visible NeV line. L_{IR}/L_{AGN} is the ratio of the integrated energy in the 8–1000 µm spectral region to the integrated energy in the QSO template from Elvis et al. (1994) when normalized to the absorption-corrected hard X-rays or X-ray upper limit (column 7) and the IRAC 8 µm photometry (column 8). The latter represents the maximum AGN contribution as it is constrained by our IR photometry. Column 9 identifies the primary energy source of the galaxy. Given the power-law-type SED of object 165, the AGN likely has a substantial contribution to the galaxy's energy budget, however the L_{IR}/L_{AGN} ratio shows that the SB component is still the primary energy source.

ID	L_{IR} class	SED type	$\log L_{2-10\,keV}(\mathrm{erg\,s^{-1}})$	[O III]/Hβ	[Ne v]	L_{IR}/L_{AGN} (X)	L_{IR}/L_{AGN} (8)	Powered by
59	LIRG	SB	42.9	7	out of range	23	10	SB
67	ULIRG	SB	43.3	out of range	yes	59	40	SB
83	LIRG	SB	42.6	too weak	out of range	42	13	SB
84	ULIRG	SB	not detected	9	out of range	2448	90	SB
114	ULIRG	SB	not detected	3	out of range	640	27	SB
122	LIRG	SB	43.4	out of range	out of range	14	13	SB
141	LIRG	SB	not detected	6	out of range	192	26	SB
165	ULIRG	power-law	not detected	8	out of range	550	6	SB /AGN
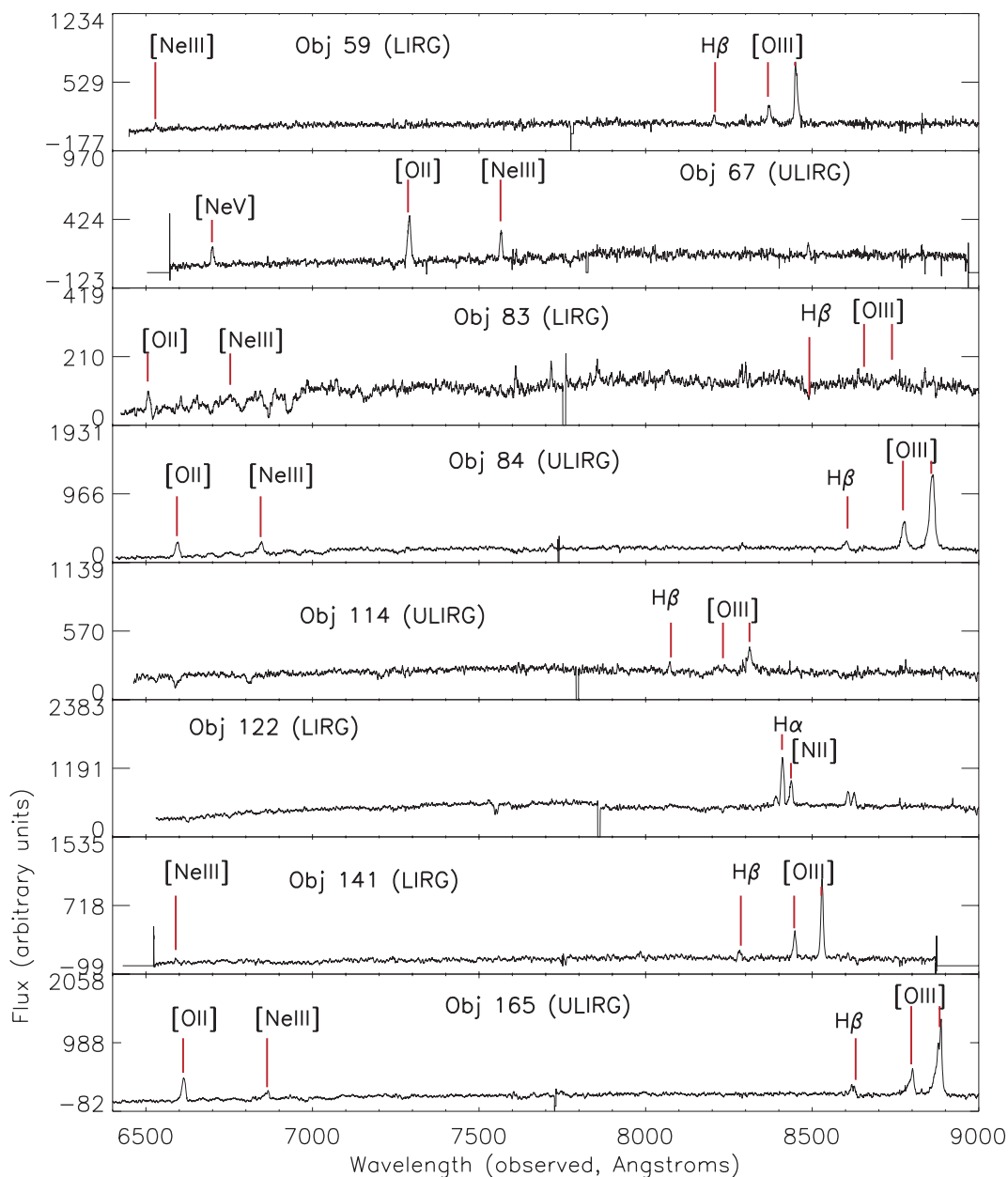
Figure 12. DEEP 2 spectra for the eight AGN candidates, whose SEDs are shown in Fig. 13.

B, *R*, *I* fluxes from DEEP 2, *J* and *K* fluxes where available, IRAC and MIPS data and the SK07 IR template best matched to each object (see Section 2.1). We use WEBPIMMS, a NASA High Energy Astrophysics Science Archive Research Center (HEASARC) tool, to estimate absorbing column densities (N_H) and correct the fluxes for absorption, via our estimated hardness ratios and a $\Gamma = 1.9$ photon index. These are shown in Table 4 where the upper and lower values for the column density are calculated using the upper and lower values of the hardness ratios. We use the average SED for a radio quiet QSO from Elvis et al. (1994) and that of a lower luminosity, lower Eddington ratio AGN, NGC 7213 from Kuraszkiewicz et al. (2003) which lacks the 'big blue bump'. Assuming that hard X-rays are a measure of AGN power, both templates are normalized to the absorption-corrected hard X-ray flux or the hard-band upper limit if either the object has no X-ray detection or it is detected only in the full band. In order to separate the AGN and host galaxy SED

components, we use templates which have little or no contribution from the host galaxy and therefore represent integrated energy from the AGN. Note that because these templates represent unabsorbed AGN, they would not be expected to match our observed spectrum in the optical/UV according to the absorbing columns we calculate. Nevertheless and assuming the unified scheme holds (Urry & Padovani 1995), the difference between an unabsorbed and an absorbed AGN SED should be far more obvious in the soft X-ray/EUV/UV and optical, whereas the contribution from the torus in the mid- and far-IR, where it is optically thin, should vary much less with orientation. Consequenctly, since our aim is to calculate the integrated AGN energy by normalizing the templates to our sources' photometry, it is not appropriate to use absorbed AGN templates where a large part of the spectrum would be partially or completely wiped out. This is particularly important for higher luminosity AGN, where most energy comes out in the UV and
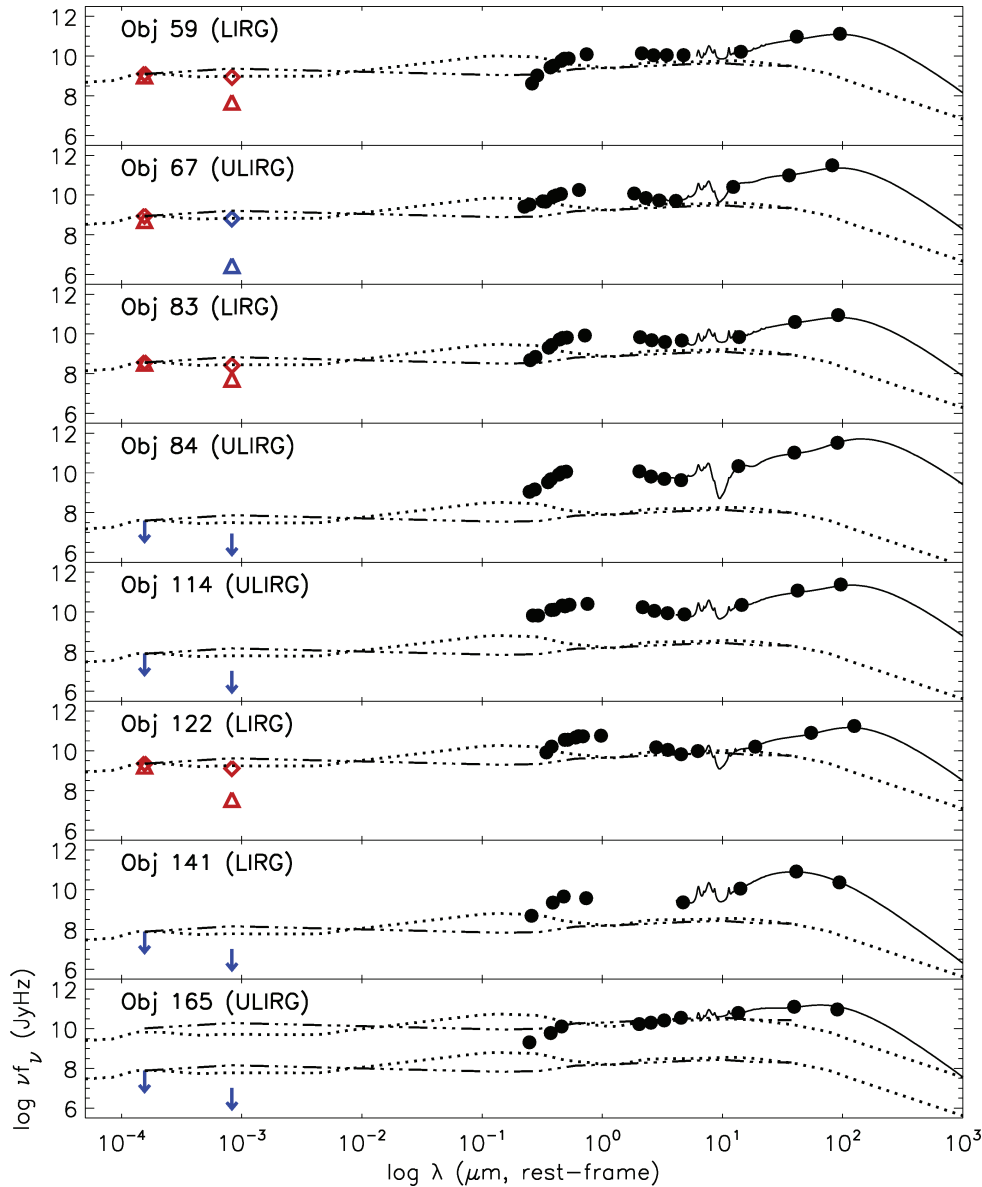
Figure 13. The X-ray to IR SEDs for the eight objects in the sample which show at least one AGN signature; black filled circles: optical/IR data, black solid line: SK07 IR model SED templates (normalized to 24 μm); dotted line: radio quiet QSO SED from Elvis et al. (1994) (normalized to the absorption-corrected hard-band X-ray flux), dash-dot line: SED of AGN NGC 7213 from Kuraszkiewicz et al. (2003) (normalized to the absorption-corrected hard-band X-ray flux), diamonds: hard and soft fluxes corrected for absorption, triangles: hard and soft fluxes not corrected for absorption (red for measured flux, blue for upper limit). When there is no X-ray detection the AGN SEDs are normalized to the hard X-ray upper limits. For object 165, which does not have an X-ray detection, but has a power-law near-IR continuum, the templates are normalized to both the hard X-ray upper limit and the near-IR continuum. [Correction added after online publication 2010 February 18: the wrong figure was originally used, and this has been corrected.]

optical. Moreover, unabsorbed templates allow us to evaluate the strength of the stellar bump in comparison to the AGN in the 1–2 μm region.

The SEDs of all eight sources (Fig. 13) are characterized by a far-IR bump significantly more luminous than the AGN templates in that part of the spectrum. For objects 84, 114 and 141 the entire optical/IR SED is displaced from the AGN templates and is two to four orders of magnitude more luminous, an indication that the AGN is of low luminosity and therefore unlikely to contribute substantially to the galaxies' energy budget. For the hard X-ray emitters, objects 59, 67, 83 and 122, the AGN templates agree better with the

mid-IR SEDs, indicating that some part of the galaxies' near/mid-IR luminosity must be coming from the AGN. Object 165 is not detected in the X-rays, but it is classed as hosting an AGN from spectral signatures and mid-IR continuum slope. Accordingly, it is more appropriate to normalize the AGN template to the near/mid-IR continuum, as the power-law SED slope in that region is characteristically emission from the torus, showing that even if the AGN is not detected in the X-rays it could be contributing substantially to the source's energy budget.

We examine the possibility that the far-IR bump results from the high-frequency light from the AGN being absorbed and

re-radiated into the IR. Assuming that X-ray emission scales with AGN power, then to power a LIRG or ULIRG ($L_{IR} = 10^{11}$–10^{13} $L_\odot$) and hence dominate emission in the far-IR, we would expect an AGN luminosity of at least a few times 10^{44} erg s^{-1}. Expecting a few per cent of that to emerge in the X-rays (e.g. Elvis et al. 1994), an X-ray luminosity of at least 10^{43} erg s^{-1} for the low-luminosity IR sources and at least 10^{44} erg s^{-1} for the more luminous LIRGs and ULIRGs is implied. None of our objects satisfies these criteria. In fact, quite simply integrating under the SEDs reveals that in all cases the IR bump (8–1000 μm) has between one and three orders of magnitude more energy than the AGN/QSO templates (defined as the L_{IR}/L_{AGN} ratio). It is possible that the column densities, and hence absorption corrections, derived from our hardness ratios could be underestimated if there is a contribution from scattered radiation in the soft X-ray band for heavily absorbed sources. In order to address this, we estimate a maximum value for L_{IR}/L_{AGN} by normalizing the AGN template to our 8 μm IRAC photometry. We find that the IR SED overtakes emission from the AGN by factors of 6–90 and hence conclude that (i) with the exception of object 165, where L_{IR}/L_{AGN} is less than an order of magnitude, for the remaining objects the AGN contributes less than 10 per cent to the IR energy budget and (ii) all sources are primarily powered by star formation – see Table 2.

5.3 Obscured AGN

Our results indicate that low-luminosity ($L_{2-10\,keV} \sim 10^{42}$ erg s^{-1}) AGN with moderate obscuration ($N_H \sim 10^{23}$ cm^{-2}) can be detected in our survey up to $z \sim 0.5$. Active nuclei obscured by higher column densities are potentially missed even if more luminous, implying that the AGN fraction that we calculate is a lower limit. Nevertheless, the hardness ratios we calculate for our stacked sources (Table 1) are soft (HR < -0.2) indicating a minor (if any) contribution from obscured AGN to the X-ray signal, making our AGN fraction relatively robust – this is further confirmed by the stacking signal from the same sample of sources minus the eight AGN candidates (see Table 3). In addition, even without X-ray detections, it is unlikely that we would misclassify AGN-powered 70-μm sources as SB dominated. As outlined in Sections 5.1 and 5.2, AGN and SB SEDs are highly divergent in the near/mid-IR and therefore if one of our $L > 10^{11}$ $L_\odot$ sources were to host a $L_{2-10\,keV} > 10^{44}$ erg s^{-1}, heavily obscured AGN which could potentially power the galaxy but is not detected in the X-rays its SED would show a strong near/mid-IR continuum: hot dust emission from the torus.

To demonstrate this further we compare the SEDs of six objects with no AGN signatures (the LIRGs and ULIRGs in Fig. 7) and AGN-candidate object 165 to the SEDs of the local IR galaxies NGC 6240 and NGC 1068 known to host Compton-thick AGN (Fig. 14). The diverse nature of NGC 6240 and NGC 1068 is un-

ambiguously mirrored in their panchromatic SEDs, which are in agreement over the optical and far-IR parts but diverge significantly in the near/mid-IR. NGC 6240 is an SB/AGN hybrid with a binary Compton-thick ($\sim 10^{24}$ cm^{-2}), $\sim 10^{44}$ erg s^{-1} QSO, but the galaxy is nevertheless primarily powered by an SB (e.g. Vignati et al. 1999; Komossa & Schulz 1999; Klaas et al. 2001), whereas NGC 1068 is a type II Seyfert ($L_{2-10\,keV} > 10^{44}$ erg s^{-1}) with an additional far-IR SB component (e.g. Le Floc'h et al. 2001; Spinoglio et al. 2005). We normalize their SEDs to the SK07 template at the IRAS 60 μm photometry, in order to be consistent with our original sample selection at 70-μm. We do not consider the soft X-ray flux, which has limited diagnostic value for such heavily obscured AGN embedded in star-forming galaxies. The hard X-ray flux we show in the SEDs of NGC 6240 and NGC 1068 is observed and hence not corrected for absorption.

We see from Fig. 14 that if there are any sources in the 70-μm sample with IR to X-ray ($L_{60\mu m}/L_{2-10\,keV}$) ratios similar to NGC 6240 and NGC 1068 then they would on average be detected in our X-ray survey. However, even if such Compton-thick AGN are missed, the near/mid-IR part of the SED would show unambiguous signatures of their presence if they were to be significant contributors to the galaxy's energy budget. Not surpisingly, apart from object 165, whose SED is better represented by that of NGC 1068, the remaining 70-μm sources are in agreement with the SB-type SED of NGC 6240.

6 SUMMARY AND CONCLUSIONS

We have investigated the nature of 61 70-μm-selected sources, by exploiting data from *Spitzer*, *Chandra* and the Keck telescopes, the latter as part of the DEEP 2 survey. In previous work, we showed that the energy budget of 70-μm-selected galaxies is defined by emission in the IR, with all $z > 0.1$ galaxies having luminosities above $L_{IR} > 10^{10}$ $L_\odot$. Our results revealed that 70-μm populations are predominantly comprised LIRGs at an average redshift of $z \sim 0.5$ and SFRs of the order of ~ 100 $M_\odot$ yr^{-1}. In addition, we found that the strong majority are identified with an SB-type SED: a well-defined optical/near-IR stellar bump, followed by an inflection at $2 \lesssim \lambda_{rest} \lesssim 6$ μm and a sharp increase in flux at IR wavelengths. The aim of the work described in this paper was to examine the X-ray and spectral properties of these sources and, by building on previous results, to develop a more detailed picture of the inherent nature of 70-μm-selected galaxies.

In order to place our sample in the context of other galaxy populations in the DEEP 2 photometric and spectroscopic survey, we evaluated its spectral properties against a control sample assembled from DEEP 2 objects of similar redshifts and optical colours (Section 2.3). The clearly identifiable stellar bump in our sources' SEDs, places them in the optically bright ($-18 < M_B < -23$)

Table 3. Table of stacked fluxes (erg s^{-1} cm^{-2}) and hardness ratios for the 70-μm sample minus the eight AGN candidates (see Section 5.1). They are split into 3 luminosity classes (SBs, LIRGs and ULIRGs; see Section 2.1 for details on the sources' IR properties). The second column indicates how many objects were used in the stacking – some were removed because they were too close to a source which could have contaminated the signal or they were associated with an X-ray source. The SB group does not have a formal detection in the hard band, so we quote the 3σ upper limit. The SB hardness ratio is derived using the counts in the soft band and 3σ upper limit counts in the hard band.

Class	Objects used	$f_{0.5-2}$	f_{2-10}	HR
SBs	eight out of 9	8.77E-17 (8σ)	2.35E-16 (3σ upper limit)	−0.3 (upper limit)
LIRGs	26 out of 31	5.93E-17 (10σ)	1.6e-16 (4σ)	−0.3
ULIRGs	9 out of 13	9.82E-17 (10σ)	2.33E-16 (3σ)	−0.4

Table 4. The 70-µm sample (61 objects): IDs from the 70-µm EGS survey and the DEEP 2 survey, redshift, R-band magnitude (AB), total IR luminosity, X-ray flux in the soft and hard bands ($\times 10^{-16}$ erg s^{-1} cm^2), hardness ratios, column density (cm^{-2}) with the upper and lower limits, line ([O II], [Ne III] Hβ, [O III]) fluxes (log W/m^2), Hδ absorption line EW (Å) and the reduced 4000 Å break. '(l)' indicates a 3σ upper limit for the fluxes. Column densities were calculated with $\Gamma = 1.9$. '(l)' in the N_H column indicates that with a $\Gamma = 1.9$ the estimated column density is lower than the Galactic N_H of $\sim 2 \times 10^{20}$. The upper and lower limits of N_H are calculated from the upper and lower values of the hardness ratio.

ID	DEEP ID	z	R mag	$L_{\mathrm{IR}} \times 10^{10}$ (L$_\odot$)	$f_{0.5-2}$	f_{2-10}	HR	N_{H}	$f_{\mathrm{[O\,II]}}$	$f_{\mathrm{[Ne\,III]}}$	$f_{H\beta}$	$f_{\mathrm{[O\,III]}}$	EW$_{H\delta}$	D_n4000
							STARBURSTS							
20	14017095	0.33	19.70	8.72±0.11	–	–	–	–	–	–	–	–	–	–
46	13056925	0.22	19.72	9.24±0.04	–	–	–	–	–	–	–	–	–	–
51	13058203	0.22	18.59	4.37±0.23	–	–	–	–	–	–	–	–	–	–
56	13041622	0.20	18.70	9.84±0.49	$9.04 \pm^{1.7}_{1.55}$	13.7(l)	$-0.48 \pm^{0.17}_{0.2}$	(l)$^{(l)}_{(l)}$	–	–	–	–	–	–
81	13009920	0.23	19.65	5.38±0.38	–	–	–	–	–	–	–	–	–	–
118	12008271	0.24	20.30	3.77±0.30	–	–	–	–	–	–	–	–	–	–
125	11051641	0.25	20.72	8.28±0.12	–	–	–	–	–	–	–	–	–	–
144	11033888	0.19	19.35	3.62±0.18	–	–	–	–	–	–	–	–	–	–
155	11020745	0.17	18.60	2.74±0.30	–	–	–	–	–	–	–	–	–	–
							LIRGs							
33	14012882	0.34	19.80	18.72±2.87	–	–	–	–	–	–	–	−19.23	–	–
37	13063596	0.36	19.49	45.23±0.46	–	–	–	–	–	–	−18.86	−19.43	–	–
40	13063597	0.30	18.36	41.96±2.10	1.75(l)	10.4(l)	$-0.24 \pm^{0.3}_{0.3}$	$5.4 \times 10^{21}\,^{1.6\times10^{22}}_{(l)}$	–	–	–	−19.70	–	–
41	14007624	0.45	20.88	80.59±7.03	–	–	–	–	–	–	−19.61	−20.06	–	–
43	13063920	0.56	20.73	32.42±3.09	$1.13 \pm^{0.97}_{0.63}$	2.23(l)	$-0.66 \pm^{0.33}_{0.08}$	(l)$^{4\times10^{21}}_{(l)}$	–	–	−19.03	−19.39	–	–
55	13049741	0.67	21.56	84.70±5.68	–	–	–	–	–	–	−19.33	−20.15	5.52	1.19
59	13050479	0.69	22.33	82.16±2.77	$4.99 \pm^{1.49}_{1.32}$	$106 \pm^{12.4}_{11.7}$	$0.61 \pm^{0.08}_{0.1}$	$1.1 \times 10^{23}\,^{1.15\times10^{23}}_{8\times10^{22}}$	–	−19.86	−19.70	−18.88	0.25	1.29
68	13034644	0.35	19.65	33.96±1.50	–	–	–	–	–	–	–	−19.12	–	–
72	13035302	0.39	20.44	13.77±1.18	–	–	–	–	–	–	–	−20.07	–	–
76	13017944	0.73	22.62	30.96±2.16	–	–	–	–	–	–	−19.54	−19.68	4.45	1.14
78	13026857	0.37	20.27	35.92±0.15	–	–	–	–	–	–	−18.91	−19.58	–	–
83	13019240	0.75	22.55	43.08±11.08	$5.53 \pm^{1.5}_{1.31}$	$35.5 \pm^{8.78}_{7.99}$	$0.15 \pm^{0.14}_{0.18}$	$4.2 \times 10^{22}\,^{5.7\times10^{22}}_{2.6\times10^{22}}$	−19.99	−20.73	–	−19.74	–	–
85	13003379	0.43	19.92	25.80±0.92	–	–	–	–	–	–	−18.82	−19.54	–	–
94	12027947	0.55	21.69	76.92±3.03	–	–	–	–	–	–	−19.17	−19.77	–	–
95	12027969	0.73	22.01	90.08±29.67	–	–	–	–	–	–	–	–	–	–
98	12023868	0.29	20.10	10.82±1.19	–	–	–	–	–	–	–	–	–	–
100	12024073	0.30	19.33	23.56±1.57	–	–	–	–	–	–	–	–	–	–
103	12029058	0.25	19.02	10.90±0.15	–	–	–	–	–	–	–	–	–	–
110	12015978	0.42	21.29	33.28±2.03	–	–	–	–	–	–	−20.42	−20.42	–	–
112	12020772	0.34	19.83	27.63±7.78	–	–	–	–	–	–	–	−19.46	–	–
115	12008273	0.38	20.08	25.12±2.17	–	–	–	–	–	–	−18.77	−19.24	–	–
120	12013167	0.57	21.61	30.13±3.76	–	–	–	–	–	–	−19.38	−19.12	–	–
121	12008914	0.78	22.07	57.08±8.60	–	–	–	–	−19.29	−19.64	−19.17	−19.49	7.77	1.1
122	12004450	0.28	19.42	11.80±2.70	$3.56 \pm^{1.51}_{1.28}$	$172 \pm^{17.9}_{16.9}$	$0.78 \pm^{0.05}_{0.07}$	$7 \times 10^{22}\,^{8\times10^{22}}_{6\times10^{22}}$	–	–	–	–	–	–
126	11051657	0.42	21.16	27.97±2.23	–	–	–	–	–	–	–	–	–	–
135	11046414	0.48	20.92	57.20±0.28	–	–	–	–	–	–	–	–	–	–
137	11046419	0.48	20.07	67.64±0.39	–	–	–	–	–	–	−18.61	−18.75	–	–
138	11039469	0.42	21.13	12.54±6.27	–	–	–	–	–	–	−19.28	−19.9	–	–
140	11047086	0.46	19.42	27.08±5.62	–	–	–	–	–	–	–	–	–	–
141	11101177	0.70	22.74	36.76±1.84	–	–	–	–	–	−20.09	−19.58	−18.79	10.14	–
146	11033882	0.46	20.05	19.64±2.18	–	–	–	–	–	–	–	–	–	–
147	11026910	0.67	22.31	85.49±14.92	$1.53 \pm^{0.88}_{0.64}$	2.58(l)	$-0.5 \pm^{0.39}_{0.2}$	(l)$^{1.8\times10^{22}}_{(l)}$	–	–	−19.74	−20.61	–	–
149	11027507	0.51	20.34	46.83±7.07	–	–	–	–	–	–	−18.52	−18.45	–	–
150	11034350	0.74	21.97	48.99±8.80	–	–	–	–	–	–	−19.44	−19.82	5.34	1.17
152	11027541	0.37	19.98	54.70±0.37	–	–	–	–	–	–	−19.19	−19.42	–	–
							ULIRGs							
24	14011285	0.76	22.07	153.57±23.59	–	–	–	–	−19.82	–	−20.28	−19.89	–	–
26	14017213	1.29	23.68	796.20±51.18	–	–	–	–	−19.38	−20.23	–	–	–	–
58	13041891	0.69	22.29	196.78±42.96	–	–	–	–	–	–	−19.67	−20.35	5.91	1.28
67	13034619	0.96	22.11	235.69±2.43	0.3(l)	$55.2 \pm^{11.9}_{10.4}$	$0.93 \pm^{0.01}_{0.07}$	$3.7 \times 10^{23}\,^{3.9\times10^{23}}_{2.8\times10^{23}}$	−19.17	−19.56	–	–	–	–
70	13026142	0.78	21.30	223.68±56.86	–	–	–	–	−19.62	−20.32	–	–	–	–
77	13036021	0.42	19.16	101.04±0.60	–	–	–	–	–	–	−18.96	−19.52	–	–
82	13027191	1.04	23.36	275.11±44.43	–	–	–	–	−19.34	−19.73	–	–	–	–
84	13019950	0.77	21.97	307.45±64.62	0.92(l)	4.2(l)	$0.32 \pm^{0.27}_{0.4}$	$6.3 \times 10^{22}\,^{1.1\times10^{23}}_{2.3\times10^{22}}$	−19.20	−19.50	−19.34	−18.39	–	–
88	13019982	0.78	21.51	254.05±10.51	–	–	–	–	−19.16	−19.51	−19.78	−19.40	–	–

Table 4 – *continued*

ID	DEEP ID	z	R mag	$L_{\mathrm{IR}} \times 10^{10}$ (L$_\odot$)	$f_{0.5-2}$	f_{2-10}	HR	N_{H}	$f_{\mathrm{[O\,II]}}$	$f_{\mathrm{[Ne\,III]}}$	$f_{H\beta}$	$f_{\mathrm{[O\,III]}}$	EW$_{H\delta}$	D_n4000
93	13004291	1.20	22.57	488.97±74.57	$1.59 \pm^{0.92}_{0.67}$	3.82(l)	$-0.34 \pm^{0.35}_{0.26}$	$1 \times 10^{22}\ ^{5\times10^{22}}_{(l)}$	−19.54	−20.50	–	–	–	–
101	12028577	0.82	23.63	100.84±12.61	–	–	–	–	–	–	–	–	–	–
114	12007915	0.66	20.83	128.59±2.51	–	–	–	–	–	–	−19.66	−19.18	–	–
124	11051625	0.85	21.31	173.78±43.18	–	–	–	–	−19.2	–	–	–	–	–
134	11038951	0.75	21.87	107.38±1.00	–	–	–	–	–	−20.30	−19.99	−19.89	–	–
158	11020790	0.93	22.08	795.07±163.23	–	–	–	–	−19.58	–	–	–	–	–
165	11014633	0.77	21.71	126.03±9.91	–	–	–	–	−19.02	−19.63	−19.35	−18.46	5.76	1.14
172	11015249	0.81	23.11	228.37±1.09	–	–	–	–	–	–	–	–	–	–
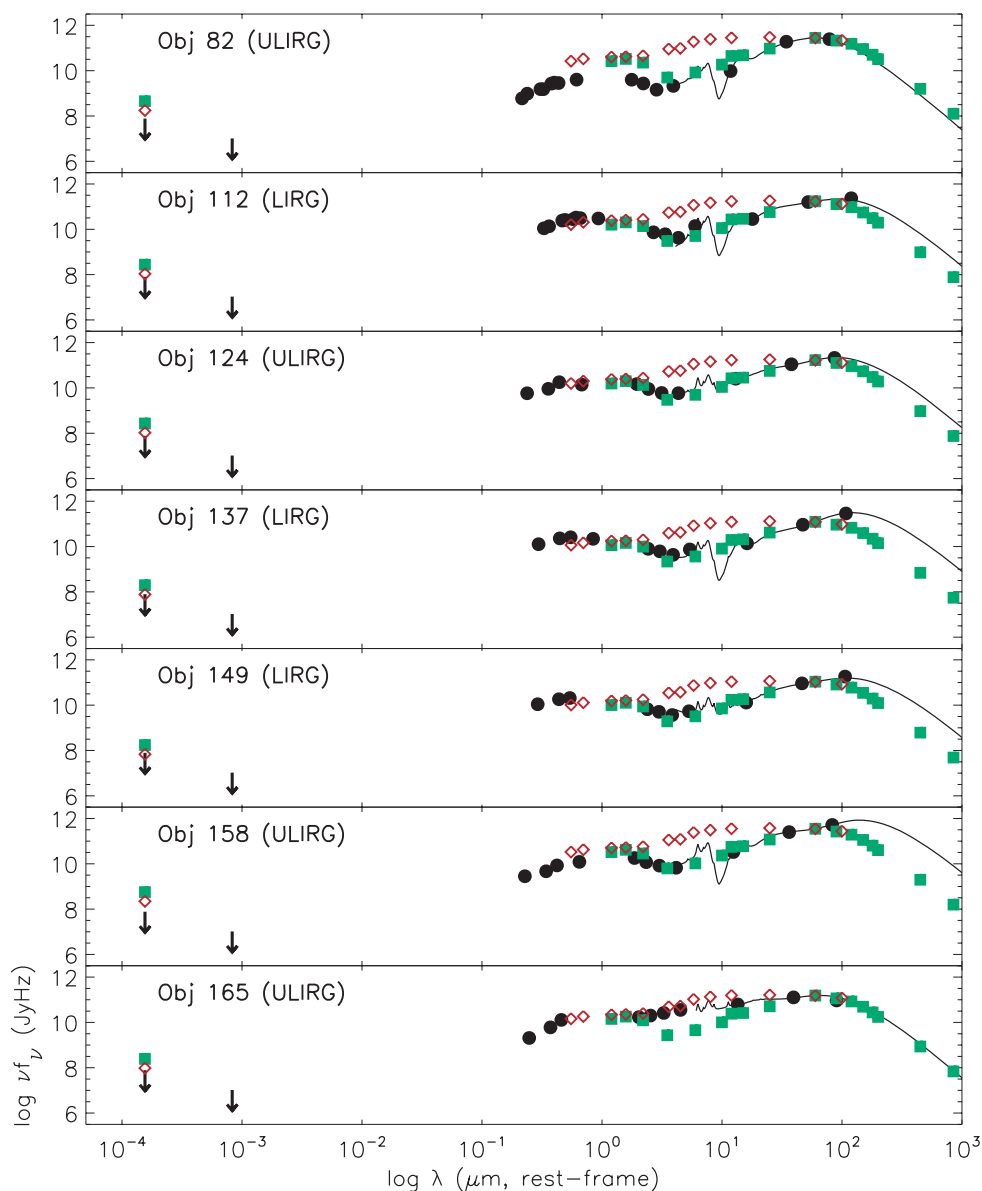
Figure 14. The X-ray to IR SEDs of 6 objects with no AGN signatures (the LIRGs and ULIRGs in Fig. 7) and AGN-candidate object 165; black upper limits: X-ray data; black filled circles: optical/IR data; black solid line: SK07 IR model SED templates (normalized to 24 μm). The red open diamonds represent the panchromatic SED of NGC 1068 – photometry for the SED from Sandage (1973), Spinoglio et al. (1995), Stickel et al. (2004), Cappi et al. (2006) and Howell et al. (2007). The green filled squares represent the panchromatic SED of NGC 6240 – photometry for the SED from Allen (1976), Soifer et al. (1989), Iwasawa & Comastri (1998), Spinoglio et al. (1995), Klaas et al. (2001) and Lutz et al. (2004). The SEDs of NGC 1068 and NGC 6240 are normalized to the SK07 template at the IRAS 60 μm photometry, in order to be consistent with our original sample selection at 70 μm. Note that for both local galaxies including the soft X-ray flux is not included, as it is dominated by emission lines from photoionized plasma, with the underlying X-ray continuum completely absorbed. The hard X-ray flux that we plot here is observed and not corrected for absorption.

and red ($0.5 < U - B < 1.5$) regime in the CMD. Our results showed that although there is agreement between some control and 70-μm galaxies, there were also evident differences in terms of both their AGN and stellar content. The [O III]/Hβ distributions of 70-μm LIRGs and respective control galaxies were in agreement with only a few outliers implying that the optically determined AGN fractions are broadly consistent in that redshift and $U - B/M_B$ range. In contrast, there was a more evident shift towards higher [O III]/Hβ for the ULIRGs than their respective control galaxies. In terms of the [Ne III]/[O II] ratio, half of the 70-μm sample was found to agree with the comparison sample, whereas half was offset towards higher values. As discussed in Section 4.2, high [Ne III]/[O II] ratios can be representative of low-metallicity systems, but also a harder ionization field, albeit not unambiguously. In terms of Hδ EWs and the Hδ−D_n4000 relation, the spread in values for the two samples show little overlap. The 70-μm population seems to be at a different evolutionary state to the control sample, undergoing intense SB episodes and characterized by younger stellar populations. This might not be surpising since, as mentioned earlier, the place of the 70-μm sample on the CMD diagram could have been affected by extinction.

Our main results are as follows.

(i) A total of 8 out of 61 sources (13 per cent of the sample) show at least one AGN signature and are therefore classed as hosting an active nucleus. The AGN fraction is 0, 11 and 23 per cent for the SB, LIRG and ULIRG groups separately, robust for $L_{2-10\,keV} > 10^{42}$ erg s^{-1} and $N_H < 4 \times 10^{23}$ cm^{-2}, but potentially an overall lower limit due to a number of lower luminosity, more heavily obscured AGN that could be missed. (Note that by AGN fraction, we simply refer to the number of sources which host an AGN). The increase with total IR luminosity is consistent with both local- and high-redshift studies (e.g. Lutz et al. 1998; Fadda et al. 2002; F03).

(ii) Seven out of the eight sources which show signatures of an active nucleus, have SEDs which are SB type with the integrated IR emission approximately one to three orders of magnitude higher than the integrated AGN emission. One object has a power-law-type SED, with a strong near/mid-IR continuum which implies that the AGN is energetically important. Obscured AGN which are possibly missed when estimating the AGN fraction are not likely to play a role when estimating the fraction of AGN-dominated sources. We estimate that for an AGN to power a LIRG or ULIRG, it must have an X-ray luminosity of at least 10^{43} erg s^{-1} and up to 10^{45} erg s^{-1}. If the central black hole activity is powerful enough to contribute substantially or even dominate the galaxy's energy budget, unambiguous AGN signatures would emerge in the near/mid-IR part of the SED, even if missed in the X-rays. As a result, we conclude that all sources in the 70-μm sample are primarily powered by star formation – this includes object 165 which has an energetically important AGN, as its far-IR SED is more luminous than the AGN component.

(iii) The X-ray detection fraction of the control sample is $4.2(\pm1.6)$ per cent, whereas for the 70-μm sources it is $16.4(\pm6.4)$ per cent. In terms of the latter, about 50 per cent comes from the objects we identified as AGN, showing a strong link between the X-ray and AGN fractions. This is to be expected, as the EGS *Chandra* survey is not deep enough to be sensitive to most of the star-forming sources in our sample. The higher X-ray, and hence, AGN incidence for the 70-μm sample is at the $\sim2\sigma$ significance level. It possibly relates to the higher estimated average stellar mass, as black hole mass is expected to scale roughly with galaxy mass, however,

it could also hint at a relation between AGN activity and star formation (e.g. see also Kauffmann et al. 2003; Silverman et al. 2009 who find a number of AGN that reside in IR-selected star-forming hosts). It remains to be seen whether the higher AGN fraction in 70μm sources is due to the higher stellar mass or the more intense star-forming activity or both.

(iv) The AGN incidence of 13 per cent that we estimate is significantly lower than what has been previously observed. Previous studies have shown that, although star formation is the dominant energy source in LIRGs and ULIRGs, a significant fraction of them host bolometrically important AGN (e.g. Solomon et al. 1997; Veilleux, Sanders & Kim 1997; Genzel et al. 1998; Downes & Solomon 1998; Scoville et al. 2000; Soifer et al. 2001; Fadda et al. 2002; Brand et al. 2006). Given this discrepancy, one would naturally ask whether there is a bias with respect to the wavelength of selection. The current status of far-IR astronomy implies that the majority of studies on the AGN content of IR galaxies have been based on populations selected in the mid-IR with the MIPS 24 μm band. As discussed in Section 5, there are fundamental differences between AGN and SB SEDs and although entirely AGN or SB-dominated objects are the extremes of this range, objects with AGN/ SB components of comparable contributions are rare and as a result sources will fall in one of the two categories. Our results have shown that a far-IR bump and an SED that peaks longwards of ~50 μm is strong evidence for the source being SB-dominated, as AGN-dominated sources peak at much shorter (near/mid-IR) wavelengths and are weak far-IR emitters (see also Alonso-Herrero et al. 2006). Consequently, one would expect a higher AGN incidence in 24 μm populations, as 24 μm a) probes emission from warm/hot dust and b) corresponds to $\lambda_{rest} \sim 13$ μm at the mean redshift of 24 μm populations ($z \sim 0.8$), where there is little relevance to ongoing star formation. It seems that setting the selection at 70 μm, at least down to the few mJy flux-density limit of our survey, enables the detection of a population of almost entirely SB-dominated galaxies. This is also consistent with recent work by Trichas et al. (2009); although the 24 μm/X-ray initial selection in Trichas et al. (2009) implies that most objects in their sample host an energetically important AGN, the additional 70-μm detection criterion results in these systems also being strongly star-forming.

ACKNOWLEDGMENTS

Kea has always had within the indigenous Hawaiian community and appreciate the opportunity to conduct observations from this mountain. We thank the anonymous referee for valuable comments.

REFERENCES

Alexander D. M., Bauer F. E., Chapman S. C., Smail I., Blain A. W., Brandt W. N., Ivison R. J., 2005, ApJ, 632, 736

Allen D. A., 1976, ApJ, 207, 367

Almaini O., Lawrence A., Boyle B. J., 1999, MNRAS, 305, L59

Alonso-Herrero A. et al., 2006, ApJ, 640, 167

Antonucci R., 1993, ARA&A, 31, 473

Appleton P. N., Charmandaris V., Gao Y., Combes F., Ghigo F., Horellou C., Mirabel I. F., 2002, ApJ, 566, 682

Baldwin J. A., Phillips M. M., Terlevich R., 1981a, PASP, 93, 5 (BPT)

Baldwin J. A., Wampler E. J., Burbridge E. M., 1981b, ApJ, 243, 76

Balogh M. L., Morris S. L., Yee H. K. C., Carlberg R. G., Ellingson E., 1999, ApJ, 527, 54

Barmby P. et al., 2006, ApJ, 642, 126

Bauer F. E., Alexander D. M., Brandt W. N., Schneider D. P., Treister E., Hornschemeier A. E., Garmire G. P., 2004, AJ, 128, 2048

Bell E. F. et al., 2004, ApJ, 608, 752

Brand K. et al., 2006, ApJ, 644, 143

Brand K. et al., 2007, ApJ, 663, 204

Brandt W. N., Hasinger G., 2005, ARA&A, 43, 827

Bruzual A. G., 1983, ApJ, 273, 105

Cappi M. et al., 2006, A&A, 446, 459

Caputi K. I. et al., 2006a, ApJ, 637, 727

Caputi K. I., Dole H., Lagache G., McLure R. J., Dunlop J. S., Puget J.-L., Le Floc'h E., Pérez-González P. G., 2006b, A&A, 454, 143

Caputi K. I. et al., 2008, ApJ, 680, 939

Coil A. L. et al., 2004, ApJ, 609, 525

Comastri A., Setti G., Zamorani G., Hasinger G., 1995, A&A, 296, 1

Conselice O. J. et al., 2007, ApJ, 660, L55

Davies R. I., Burston A., Ward M. J., 2002, MNRAS, 329, 367

Davis M. et al., 2003, Proc. SPIE, 4834, 161

Davis M. et al., 2007, ApJ, 660, L1

Donley J. L., Rieke G. H., Rigby J. R., Pérez-González P. G., 2005, ApJ, 634, 169

Downes D., Solomon P. M., 1998, ApJ, 507, 615

Draine B. T., 2003, ARA&A, 41, 241

Dressler A., Gunn J. E., 1983, ApJ, 270, 7

Dwek E., 1986, ApJ, 302, 363

Elvis M. et al., 1994, ApJS, 95, 1

Fabbiano G., 1989, ARA&A, 27, 87

Faber S. M. et al., 2007, ApJ, 665, 265

Fabian A. C., Iwasawa K., 1999, MNRAS, 303, L34

Fabian A. C., Barcons X., Almaini O., Iwasawa K., 1998, MNRAS, 297, L11

Fabian A. C., Wilman R. J., Crawford C. S., 2002, MNRAS, 329, L18

Fadda D., Flores H., Hasinger G., Franceschini A., Altieri B., Cesarsky C. J., Elbaz D., Ferrando P., 2002, A&A, 383, 838

Ferreras I., Lisker T., Pasquali A., Khochfar S., Kaviraj S., 2009, MNRAS, 396, 1573

Firth A. E. et al., 2002, MNRAS, 332, 617

Franceschini A. et al., 2003, A&A, 403, 501 (F03)

Genzel R. et al., 1998, ApJ, 498, 579

Georgakakis A. et al., 2006, MNRAS, 371, 221

Georgakakis A., Rowan-Robinson M., Babbedge T. S. R., Georgantopoulos I., 2007, MNRAS, 377, 203

Gregorich D. T., Neugebauer G., Soifer B. T., Gunn J. E., Herter T. L., 1995, AJ, 110, 259

Griffiths R. E., Padovani P., 1990, ApJ, 360, 483

Hasinger G., 2008, A&A, 490, 905

Ho L. C., Filippenko A. V., Sargent W. L. W., 1997, ApJ, 487, 579

Ho P. T. P., Turner J. L., Fazio G. G., Willner S. P., 1989, ApJ, 344, 135

Howell J. H. et al., 2007, AJ, 134, 2086

Imanishi M., Dudley C. C., Maiolino R., Maloney P. R., Nakagawa T., Risaliti G., 2007, ApJS, 171, 72

Iwasawa K., Comastri A., 1998, MNRAS, 297, 1219

Iwasawa K., Matt G., Guainazzi M., Fabian A. C., 2001, MNRAS, 326, 894

Kauffmann G. et al., 2003, MNRAS, 341, 33

Kewley L. J., Geller M. J., Jansen R. A., 2004, AJ, 127, 2002

Kim D.-W., Fabbiano G., Trinchieri G., 1992a, ApJS, 80, 645

Kim D.-W., Fabbiano G., Trinchieri G., 1992b, ApJ, 393, 134

King A., 2005, ApJ, 635, L121

Klaas U. et al., 2001, A&A, 379, 823

Komossa S., Schulz H., 1999, Ap&SS, 266, 61

Kuraszkiewicz J. K. et al., 2003, ApJ, 590, 128

Lacy M. et al., 2004, ApJS, 154, 166

Laird E. S., Nandra K., Adelberger K. L., Steidel C. C., Reddy N. A., 2005, MNRAS, 359, 47

Laird E. S. et al., 2009, ApJS, 180, 102 (L09)

Le Floc'h E., Mirabel I. F., Laurent O., Charmandaris V., Gallais P., Sauvage M., Vigroux L., Cesarsky C., 2001, A&A, 367, 487

Lutz D., Maiolino R., Spoon H. W. W., Moorwood A. F. M., 2004, A&A, 418, 465

Lutz D., Spoon H. W. W., Rigopoulou D., Moorwood A. F. M., Genzel R., 1998, ApJ, 505, L103

Magorrian J. et al., 1998, AJ, 115, 2285

Marcillac D., Elbaz D., Chary R. R., Dickinson M., Galliano F., Morrison G., 2006, A&A, 451, 57

Martínez-Sansigre A., Rawlings S., Lacy M., Fadda D., Jarvis M. J., Marleau F. R., Simpson C., Willott C. J., 2006, MNRAS, 370, 1479

Martínez-Sansigre A., Rawlings S., Lacy M., Fadda D., Marleau F. R., Simpson C., Willott C. J., Jarvis M. J., 2005, Nat, 436, 666

Matute I., La Franca F., Pozzi F., Gruppioni C., Lari C., Zamorani G., 2006, A&A, 451, 443

Nagao T., Maiolino R., Marconi A., 2006, A&A, 459, 85

Nagao T., Murayama T., Shioya Y., Taniguchi Y., 2002, ApJ, 567, 73

Nandra K., Mushotzky R. F., Arnaud K., Steidel C. C., Adelberger K. L., Gardner J. P., Teplitz H. I., Windhorst R. A., 2002, ApJ, 576, 625

Neugebauer G., Oke J. B., Becklin E. E., Matthews K., 1979, ApJ, 230, 79

Norman C., Scoville N., 1988, ApJ, 332, 124

Osterbrock D. E., 1989, New York Academy Sciences Annals, 571, 99

Pérez-Montero E., Hägele G. F., Contini T., Díaz Á. I., 2007, MNRAS, 381, 125

Pérez-Montero E. et al., 2009, A&A, 495, 73

Pompilio F., La Franca F., Matt G., 2000, A&A, 353, 440

Ptak A., Heckman T., Levenson N. A., Weaver K., Strickland D., 2003, ApJ, 592, 782

Ranalli P., Comastri A., Setti G., 2003, A&A, 399, 39

Rieke G. H. et al., 2004, ApJS, 154, 25

Rowan-Robinson M., 1995, MNRAS, 272, 737

Rowan-Robinson M., Crawford J., 1989, MNRAS, 238, 523

Sandage A., 1973, ApJ, 183, 711

Sanders D. B., Soifer B. T., Elias J. H., Neugebauer G., Matthews K., 1988, ApJ, 328, L35

Scoville N. Z. et al., 2000, AJ, 119, 991

Setti G., Woltjer L., 1989, A&A, 224, L21

Shanks T., Georgantopoulos I., Stewart G. C., Pounds K. A., Boyle B. J., Griffiths R. E., 1991, Nat, 353, 315

Siebenmorgen R., Krügel E., 2007, A&A, 461, 445

Silverman J. D. et al., 2009, ApJ, 696, 396

Soifer B. T., Boehmer L., Neugebauer G., Sanders D. B., 1989, AJ, 98, 766

Soifer B. T. et al., 2001, AJ, 122, 1213

Solomon P. M., Downes D., Radford S. J. E., Barrett J. W., 1997, ApJ, 478, 144

Spergel D. N. et al., 2003, ApJS, 148, 175

Spinoglio L., Malkan M. A., Rush B., Carrasco L., Recillas-Cruz E., 1995, ApJ, 453, 616

Springel V., Di Matteo T., Hernquist L., 2005, MNRAS, 361, 776

Stern D. et al., 2005, ApJ, 631, 163

Stickel M., Lemke D., Klaas U., Krause O., Egner S., 2004, A&A, 422, 39

Sturm E., Lutz D., Tran D., Feuchtgruber H., Genzel R., Kunze D., Moorwood A. F. M., Thornley M. D., 2000, A&A, 358, 481

Symeonidis M. et al., 2007, ApJ, 660, L73 (S07)

Symeonidis M., Page M. J., Seymour N., Dwelly T., Coppin K., McHardy I., Rieke G. H., Huynh M., 2009, MNRAS, 397, 1728 (S09)

Symeonidis M., Willner S. P., Rigopoulou D., Huang J.-S., Fazio G. G., Jarvis M. J., 2008, MNRAS, 385, 1015 (S08)

Tacconi L. J., Genzel R., Lutz D., Rigopoulou D., Baker A. J., Iserlohe C., Tecza M., 2002, ApJ, 580, 73

Takata T., Sekiguchi K., Smail I., Chapman S. C., Geach J. E., Swinbank A. M., Blain A., Ivison R. J., 2006, ApJ, 651, 713

Tresse L., Rola C., Hammer F., Stasińska G., Le Fevre O., Lilly S. J., Crampton D., 1996, MNRAS, 281, 847

Trichas M., Georgakakis A., Rowan-Robinson M., Nandra K., Clements D., Vaccari M., 2009, MNRAS, 399, 663

Umemura M., Fukue J., Mineshige S., 1997, ApJ, 479, L97+

Urry C. M., Padovani P., 1995, PASP, 107, 803

Veilleux S., Osterbrock D. E., 1987, ApJS, 63, 295

Veilleux S., Sanders D. B., Kim D.-C., 1997, ApJ, 484, 92

Vignati P. et al., 1999, A&A, 349, L57

Werner M. W. et al., 2004, ApJS, 154, 1

Willmer C. N. A. et al., 2006, ApJ, 647, 853

Worsley M. A. et al., 2005, MNRAS, 357, 1281

This paper has been typeset from a TeX/LaTeX file prepared by the author.